Optimized 3D-printing of Carbon Fiber-Reinforced Polyether-ether-ketone (CFR-PEEK) for Use in Overmolded Lattice Composite

A Thesis Presented for the
Master of Science
Degree
The University of Tennessee, Knoxville

Ryan Ogle
December 2022

ABSTRACT

Current orthopedic implants are overwhelmingly composed from metallic materials. These implants show superior mechanical properties, but this can additionally result in stress shielding due to a modulus mismatch between the bone tissue and implanted device. Polymeric implants reduce this stress shielding effect but have much lower mechanical properties, limiting their use. Polylactic acid (PLA) is a widely used biodegradable thermoplastic polymer, however, its use has been limited by the polymer's mechanical properties and rapid loss of strength during degradation in vivo. Polyether-ether-ketone (PEEK) is another common biocompatible polymer , with chemical and mechanical properties which make it a popular alternative to metallic implants. The ability to 3D print carbon fiber-reinforced PEEK (CFR-PEEK) components with the relatively cheap fused filament fabrication (FFF) process furthers the favorability of this polymer. By incorporating the stronger CFR-PEEK as a reinforcing lattice structure, the properties of biodegradable polymer can be improved. 3D-printed lattices have been extensively researched, but they have yet to be investigated as the reinforcing component of an overmolded composite. The purpose of this work is to develop a novel overmolded lattice (OML) composite. This was accomplished by first optimizing the print parameters to maximize interlayer adhesion (ILA) using a proposed redesigned tensile specimen. These results were then used to print CFR-PEEK gyroid and then injection overmolded with PLA and characterized via flexural testing. The results of the parameter optimization showed increases in ILA with increased print temperature, print speed, and reduced layer height. The flexural results of the OML showed specific flexural strength (SFS), specific

flexural modulus (SFM), and specific energy absorption (SEA), compared to the PLA and the CFR-PEEK gyroid lattice. The overmolded composite was found to have properties comparable to CFR-PEEK and had a SFM (4.3GPa/g) which exceeded all other materials tested. This composite structure has the potential to be integrated in a number of applications to provide highly tailored reinforcement of a weaker polymer matrix.

TABLE OF CONTENTS

LIST OF TABLES

LIST OF FIGURES

CHAPTER ONE

INTRODUCTION AND BACKGROUND INFORMATION

Orthopedic Biomaterial Design Considerations

Determining the optimal implant design requires an understanding of the bone tissue and the processes by which it heals and maintains itself. Bone tissue can be understood in a basic form as a composite structure comprised of an organic phase and a larger inorganic phase. The organic phase is primarily composed of type I collagen, while the inorganic phase is a calcium phosphate ceramic- primarily hydroxyapatite ($Ca10(PO4)_6(OH)_2$)-, with additional non-collagenous proteins, lipids, and water in much smaller amounts [1]–[3]. The primary effector cells in the maintenance and repair of these tissues are osteoclasts and osteoblasts. The activity of these cells can be induced by the mechanical and chemical stimuli in the cells' environments.

The adaptive response of bone tissue to mechanical stimuli is generally referred to as Wolff's Law [4]–[6]. Since the formal conception of this principle over a century ago [7], several criticisms have arisen that this "law" is actually comprised of a number of separate underlying processes which are better understood apart from each other [4]. For the present purpose of this work, however, the basic foundational understanding will suffice. In short, Wolff's Law describes the inductive action of mechanical stimuli in the bone remodeling process and selective deposition of new bone tissue. This applied load translates into strain experienced in the bone tissue, and ultimately by the appropriate effector cells.

Orthopedic implants have traditionally been dominated by metallic devices. The metals most commonly used include titanium- in both pure and alloyed forms-, cobalt-chromium (Co-Cr) alloys, and surgical grades of stainless steel [8]–[10]. As Millis (2014) highlights, the clear benefit of these metals is the sufficient load-bearing capability they provide to "allow early weight bearing and patient mobility", but at a cost of reduced physiologic loading, improper healing, and possibly necrosis of the tissue [11]. Any of these common metals will have a Young's modulus significantly greater than that of cortical bone [10], [12]. Titanium possesses a relatively low modulus of about 110 GPa, whereas the moduli of Co-Cr and stainless-steel alternatives can be roughly twice that [8], [10]. Even this modulus value, however, is considerably greater than the typical range for cortical bone (15-30 GPa) [8], [9], [12]–[14]. A significant modulus mismatch between the implant and bone tissue causes a stress-shielding effect [8], [9], [13], [15]. Consequently, loads are not effectively transferred throughout the bone tissue as it would without the implanted device, leading to a loss of bone mass and higher likelihood of fracture [16].

Several methods have been explored to improve osseointegration with titanium (Ti-6Al-4V) and stainless steel (316L). These methods include surface modifications (e.g., adding surface roughness/textures), adding bioactive coatings, and the release of bioactive agents [17]. Despite these advancements, corrosion of these metals is still of particular concern. The risk of developing cutaneous and systematic hypersensitivity reactions is increased with long-term lifespan of these devices [9]. Ivanova et al. (2014)

provide a thorough overview of some ways in which the metal debris produced could lead to systemic toxicity damage to the patient, given sufficient exposure [18].

Polymeric Implants

Polymers are widely used for medical applications and implants. Driving factors promoting the use of these polymers in medicine include ease of manufacturing and modification [19]. The benefits of polymeric implants include the ability to tailor the mechanical properties and bioactive effect on cells for the desired application. Typical polymeric biomaterials and their applications have been thoroughly reviewed elsewhere and will not be covered other than the materials involved in the present work [20], [21].

Biocompatible polymers can be generally classified by whether they undergo degradation *in vivo*. If the implant is expected to degrade, the physiological impact of any degradation products must be considered [21]. Aliphatic polyesters are particularly common materials for tissue engineering (TE), due to their safe degradation and tunable properties [22], [23]. Polylactic acid (PLA) is one such biodegradable polyester which has been approved by the Food and Drug Administration (FDA) and has been the subject of extensive research. When PLA is implanted *in vivo*, the polymer degrades via hydrolysis into α-hydroxy acid which is subsequently removed from the body through normal cellular functions [24]. There is concern, however, for the potential of a local acidosis effect due to an accumulation of the degradation products [17]. This acidic cellular environment could result in inflammation and impact bone growth. Osteoclastic activity has been shown to be dependent on the pH of the cellular environment [25], [26]. Acidosis results in increased bone resorption in order to release the alkaline components

in order to raise the local pH. The resorption of bone mineral is the greatest at a pH of 6.8 and nearly stops as that value increases to 7.4 [27]. PLA is already used for orthopedic applications, however, the low toughness of the material has been identified as a limiting factor [24].

Another biomedical polymer of particular interest is polyether-ether-ketone (PEEK), an organic semicrystalline thermoplastic polymer [28]. Compared to the moduli of the typical permanent orthopedic metals, the elastic modulus of PEEK (3-4 GPa) is significantly closer to that of cortical bone (6-30 GPa) [29]. Consequently, PEEK implants have the potential to greatly reduce stress shielding and improve tissue repair [15], [16], [29]. Sagomonyants et al. (2008) found the bone-forming capacity of PEEK *in vitro* to be comparable to that of rough titanium [16]. PEEK is biocompatible and bioinert due to its excellent chemical resistance, making it well-suited for long-term durability *in vivo* [30]. The crystalline melting temperature of PEEK is 343°C, with a degradation onset temperature of 575-580°C [31]. The chemical and thermal stability of PEEK allows these devices to withstand sterilization via steam, gamma, beta, and X-ray [15], [32], [33]. The high melting temperature of PEEK also makes it a good candidate for overmolding applications. Implants made of PEEK do not introduce any medical imaging artifacts due to the materials radiolucent nature [15], [29]. The material properties of PEEK makes it an appropriate polymer matrix for carbon fiber (CF) composites [34].

Additive Manufacturing

Additive manufacturing (AM) is a technology with immense potential and growing interest in a wide range of industries [28], [35]. While AM can refer to an array

of different additive methods (e.g., stereolithography (SLA), selective laser melting (SLM)), the market size for all major AM methods have seen sustained growth, with a projected compound annual growth rate of more than 20% [36]–[38]. One such projection of this market is illustrated in Fig. 1.1 [39].These additive technologies allow for cost-effective fabrication of highly complex structures which may not be possible to easily replicate using traditional subtractive manufacturing methods [35], [40]. While AM has been integrated and extensively researched in an array of industrial and commercial applications, the relative novelty of the technology should not be overlooked. The first 3D-printing prototype was developed less than 40 years ago, with widespread consumer accessibility only beginning around 2009 [41].

A Brief History of Additive Manufacturing

The origin point for 3D printing can be set at a number of events depending on individual distinctions of significance. For example, the concept of a 3D printing machine was first published in the 1945 short story “Things Pass By” by Leinster [41]. The origin most commonly referred to, however, is generally the development of the first 3D printer in 1984 by Hull [28], [42]–[44]. Hull invented and patented SLA printing in this accomplishment, which lead to a series of other developments and patents of similar additive methods. Just 5 years later, Crump and Crump invented and patented the fused deposition modeling (FDM) process and subsequently founded Stratasys Inc. [42], [43]. Since then, a variety of advancements has made FDM printing significantly more efficient and inexpensive, quickly establishing it as the most popular method for desktop 3D printers [42], [43], as well as the most common AM method for thermoplastic

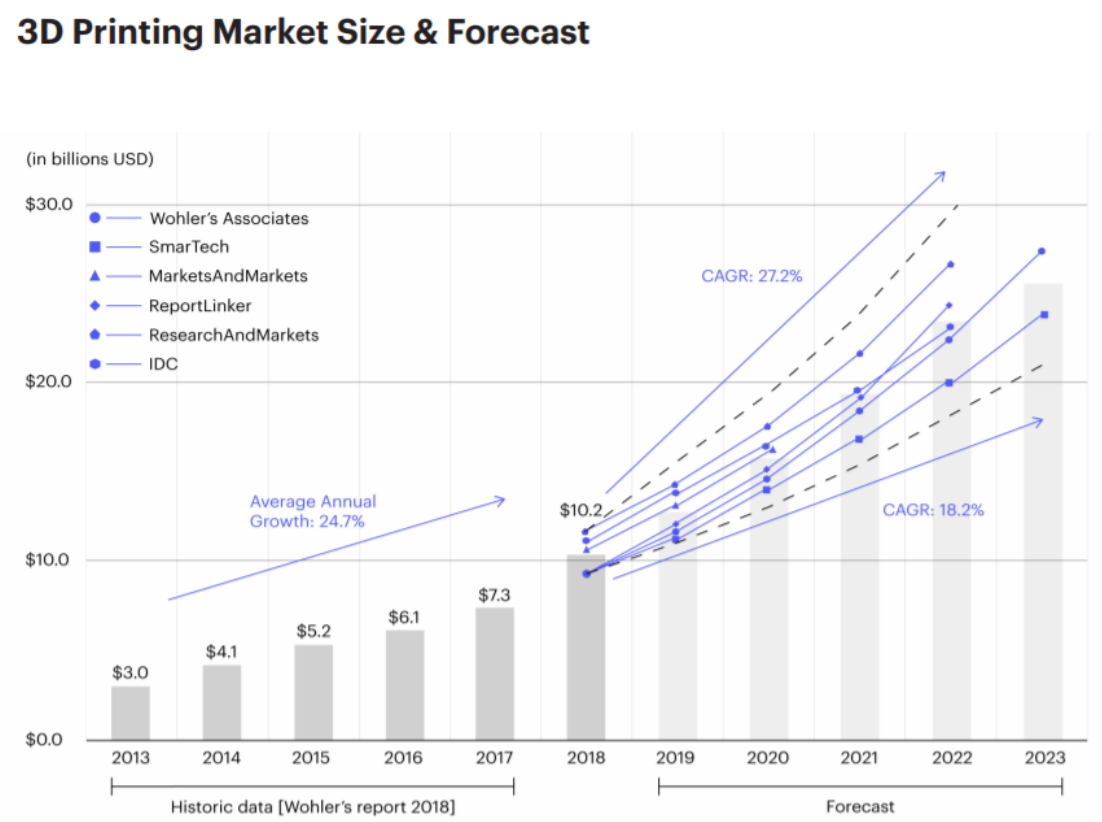

Figure 1.1 – Observed and projected growth of 3D printing market. The market is expected to double in size every 3 years as the technology is increasingly used in manufacturing applications [39].

polymers [45]. It is worth noting, within the 3 years prior to Hull's development, both Kodama in Japan, and a group of French inventors attempted to file patents for similar rapid prototyping devices, but neither was granted due insufficient funding [46].

Understanding the dramatic shift in accessibility to 3D printing on a consumer level cannot be done without emphasizing the role Bowyer and the RepRap project played [47]. The purpose of the RepRap project was to develop an inexpensive open-source design for a self-replicating 3D printer to enable accessibility for non-industrial users. RepRap (Replicating Rapid-prototyper)- invented in 2004 by Bowyer- has its origin in a project at the University of Bath [48], [49]. The motivation for this work was the prohibitive costs of commercially available 3D printers - the cheapest of which in 2007 was still nearly $10,000 [48], [50]. Once the patent held by Stratasys expired in 2009, this price dropped to less than $1,000 [51].

For clarity when discussing this technology, it is worth noting the distinction between the similar terminology commonly used. While the patent held by Stratasys for this technology has expired, the FDM term remains trademarked by the company [41], [52]. The term fused filament fabrication (FFF) was coined by those involved in the RepRap project to provide an untrademarked substitute [53]. Despite the legal status of the term, FDM is more widely recognized and commonly used to refer to FFF printers as well. While FDM and FFF are effectively interchangeable now, given the context detailed in this section, the term FFF will be preferred in this work to ensure terminological accuracy.

Fused Filament Fabrication (FFF)

FFF printing, in its current state, has been established as a reliable and relatively inexpensive process when considering initial investment, material costs, and low maintenance requirements [28]. The FFF process has been largely adopted for prototype fabrication applications due to the short cycle times, inexpensive manufacturing costs, and minimal material waste and required post-processing [28], [54]–[56]. In addition to research and industry applications, the accessibility of this technology has made it ideal for many hobbyists. Consequently, this level of accessibility has promoted a general interest in this technology both on the industrial and consumer level. In fact, a 2017 global survey of additive users covering an array of industries found both plastics to be the most common 3D printing material, and FDM as the most used AM method, followed by SLS [55], [56].

The most common FFF materials include polylactic acid (PLA), acrylonitrile butadiene styrene (ABS), polyethylene terephthalate (PETG), but there has been a growing interest in FFF-printing high performance polymers [57]. While AM technologies have been increasingly incorporated in more manufacturing applications, FDM has been limited by a few key factors. These factors can include concerns over material anisotropy and limited standardized characterization methods specific to FFF. The former is covered here, while the latter is reviewed in a later section.

Parts fabricated via the FFF printing are known to possess inherently orthotropic mechanical properties [55], [58]. The mechanical behavior and structure of FFF components can be treated as a laminar composite with stacked layers of bonded fibers

[59]. The cause of this observed anisotropy is due to the failure of the adhesion forces binding the individual printed filament segments together. The overall strength of FFF-printed parts is a combination of the polymers material properties and these bonding forces formed during fabrication [60]. The images and corresponding graph presented in Fig. 1.2 illustrates the mechanics as well as the importance of considering filament orientation relative to the desired mechanical properties. The failure seen is due to a combination of delamination and tensile failure of individual printed filament segments. The contour layers remained intact while the infill layers fractured due to the alternating layers oriented 0° and 90° relative to the loading direction. Such a failure mode does not effectively isolate the properties of the printed filament, or the bonding forces between them.

The two general bonding forces responsible for the integrity of these structures can be described as intralayer adhesion, interlayer adhesion (ILA). The ILA forces are generally similar to or less than intralayer adhesion due to increased cooling time before bonding with the next printed layer. Both forces, however, are significantly weaker than the expected tensile strength of the material. Because of this, the highest tensile strength can be expected when loaded parallel to the filament orientation [54], [59]. Conversely, FFF components commonly fail due to delamination of these discrete layers. This effect is more pronounced in semicrystalline polymers (e.g., PEEK) [32]. This illustrates these bonding forces- and specifically the ILA force- as a significant limiting factor for the mechanical properties of FFF parts. The interface between layers becomes a natural weak point of FFF-printed structures, and a clear way to improve the strength of these parts is

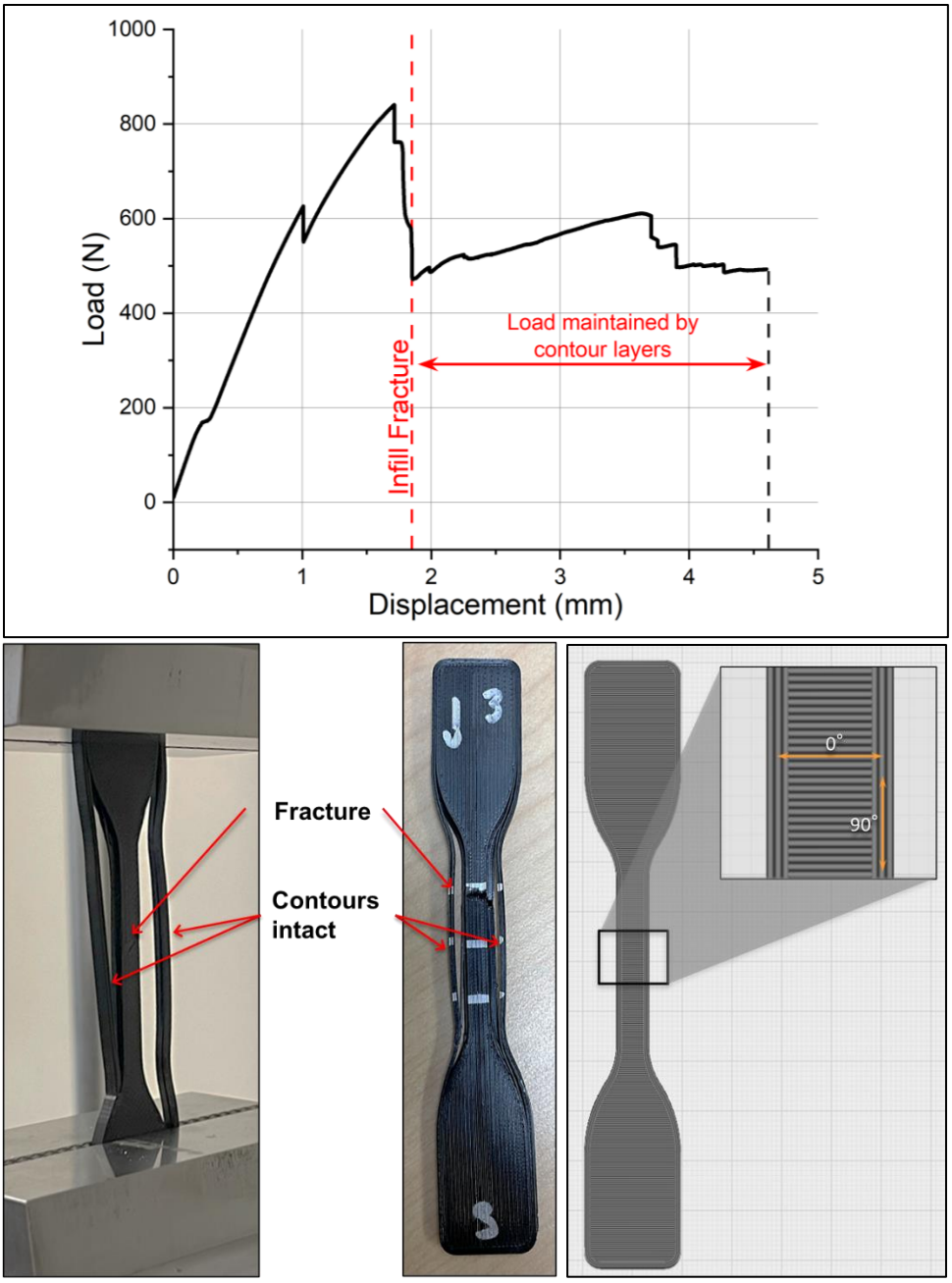

Figure 1.2 – Illustration of an undesirable tensile failure due improper filament orientation. Load-displacement curve showing the failure of the infill body and continued loading of contours (top), images showing the corresponding fracture and contour delamination of the specimen (bottom left), and the expected directions of tensile strength according to filament direction (bottom right). The tensile samples were printed with alternating 0° and 90° layers.

to maximize the adhesion between the layers.

Lattice Structures and Scaffolds

As a result of the rapid advancements in AM, highly complex structures can now be fabricated with a high level of precision which was previously impossible with alternative manufacturing methods [61]. These structures have been used for weight reduction, energy absorption, heat dissipation, osseointegration, and vibrational and acoustic damping [62]–[64]. While it is possible to produce these cellular structures using conventional subtractive methods, the capabilities are limited and typically require post-processing and an increase in material waste [62]. Fabricating these lattices via AM allows for improved manufacturing efficiency, resulting in shorter manufacturing times, reduced material waste, and a greater flexibility of design [62]. These structures can additionally allow for improved design optimization by tailoring the lattice design and morphology in order to tune a number of properties for the desired application [65].

Lattice structures can vary significantly in morphology, with no unified definition or classifications [62]. An article from *nTopology* classifies the variety different lattice structures into 4 categories: beam, plate, triply-periodic minimal surface (TPMS), and stochastic lattices [64]. An example of each of these lattice types is provided in Fig. 1.3.

The stochastic lattice is the only type of the four which is non-periodic. A popular example of this type of structure is the Voronoi lattice, the design of which is generated using the Voronoi tessellation method [66], [67]. These non-periodic lattices have been of particular interest for bone tissue engineering (BTE). The stochastic design can be

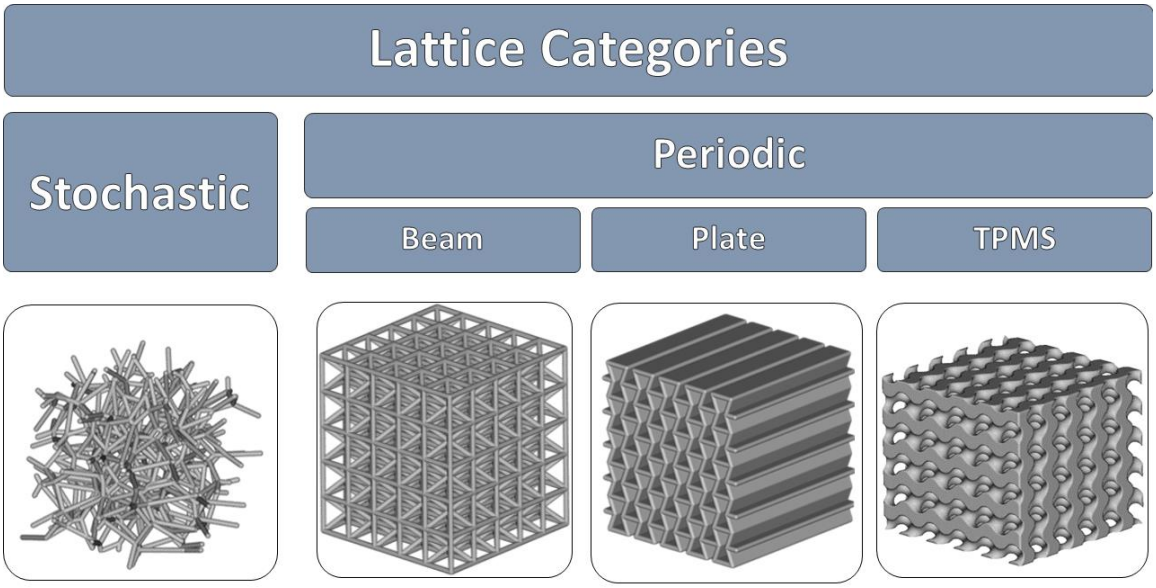

Figure 1.3 – Types of lattice structures following classifications provided by *nTopology* [64]. Lattice examples of each type from left to right are Voronoi, IsoTruss, reentrant honeycomb, and gyroid. All latices generated in 40mm cube volume.

modified to match more closely the morphology and mechanical properties of cancellous bone tissue [68]. Biomimetic designs with morphologies similar to cancellous bone has been shown to translate to overall improved tissue development and reduced stress shielding [62], [69]. The random nature of these Voronoi lattices, however, makes the prediction of mechanical properties to be more complex than periodic structures [68], [70].

Strut-based lattices are popular periodic structures to reduce material weight and improve specific strength. These lattices are typically stretching-dominant structures, allowing them to provide high specific stiffness as well. Many are these lattices are not ideal for FFF printing due to the lack of layer connectivity. The discretization of the individual struts into printable layers results in poor layer connectivity. The geometry of these struts typically provides very little surface area between layers to maximize ILA when compared to minimal surfaces. Increasing the strut thickness can increase the surface area of the layer, however, this variation of this value is generally greater than those of both plate and TPMS lattices. This increased variation creates inherent weak points as it relates to its effect on ILA.

Plate lattice structures- such as the popular honeycomb lattice- provide good specific strength and stiffness when loaded axially along the length of the lattice cells. The unidirectional architecture of these lattices additionally provides consistent layer surface areas. For any plate lattice architecture composed of a single extruded length of a 2D-profile, the layer area- and the ILA as a result- is expected to be consistent throughout the structure. The mechanical support is significantly reduced when loaded laterally

giving these lattices an anisotropic nature. Additionally, the lack of interconnectivity between cells in plate lattices reduces their efficacy in TE and overmolding applications.

TPMS lattices are based on mathematical formulas. TPMS lattices have higher surface-to-volume ratio than beam lattices [71]. TPMS lattices have high specific stiffness, axisymmetric stiffness, and pore connectivity [62], [63]. Examples of naturally occurring minimal surfaces have been found, reinforcing the argument their efficacy in TE applications [72]. A well-known example of these minimal surfaces is the gyroid structure. The evolution of a gyroid surface is illustrated in Fig. 1.4. The surface of a gyroid is approximated by Eq. 1, where a is the periodicity of the surface [73].

$$\sin(2\pi xa)\cos(2\pi ya) + \sin(2\pi ya)\cos(2\pi za) + \sin(2\pi za)\cos(2\pi xa) = 0 \qquad (1)$$

The gyroid lattice is a bending-dominant lattice with isotropic stiffness properties [74], [75]. The continuous smooth curvature of these lattices further their potential compatibility with the FFF process. The stacked layer geometries only gradually vary from one another, proving a high level of printability. By the mathematical definition of the gyroid, the CSA of each lattice is expected to be maintained at a constant value, providing homogenous ILA throughout the printed lattice.

For all of these lattice types, each can be functionally graded to further optimize the design for the desired properties. These modifications can include varying beam thickness or cell size, conformal morphologies, or a combination of different morphologies [78] . Two examples of such modifications are illustrated in Fig. 1.5.

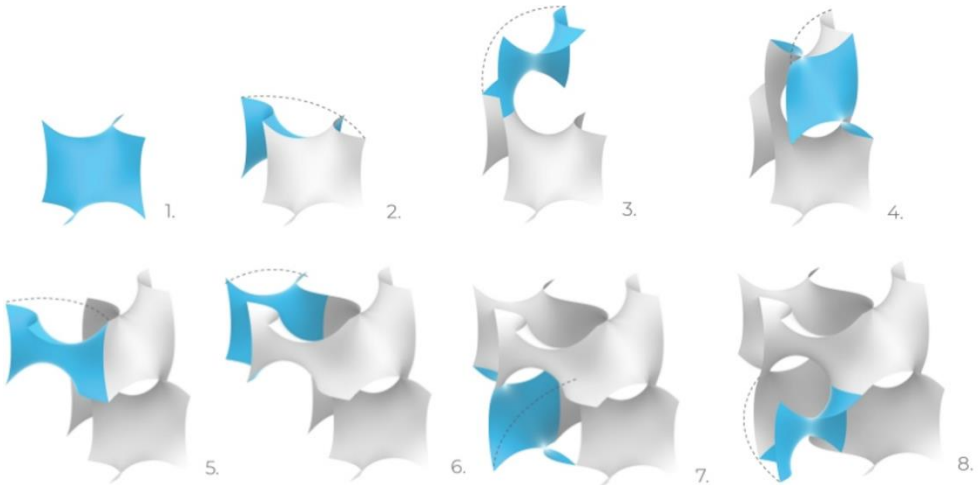

Figure 1.4 – Evolution of a gyroid surface [76], [77]

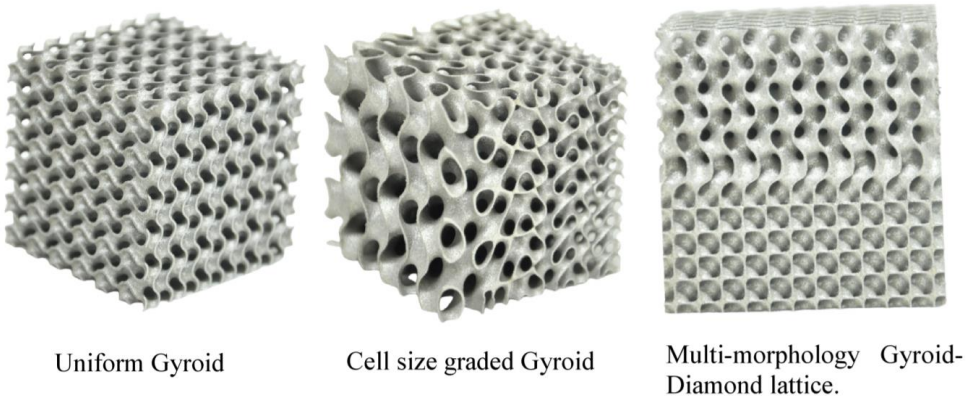

Figure 1.5 – Examples of functionally graded metallic TPMS lattices. Generated with *MSLattice* [78].

Lattice Structures as Tissue Scaffolds

For the field of BTE, the design of the lattice must include additional considerations for use as a tissue scaffold. These can be generally classified as mechanical, chemical, and physiological considerations. As mentioned in previous sections, the ideal implant would approximately match the elastic modulus of the tissue to minimize stress shielding, and both the material and any degradation products must be biocompatible. The physiological considerations include the design aspects which allow for the necessary cellular functions of the tissue regeneration. For example, the morphology should be an open interconnected porous structure to allow for vascularization and cell mobility throughout the scaffold [79]. The design should additionally have a large surface-to-volume ratio in order to maximize the potential for cell adhesion [80]. Also included are the design elements incorporated to improve bioactivity. These could be additives encapsulated into a biodegradable polymer as well as surface modifications to elicit a desired cellular response.

Sequence of Document

There has been an extensive amount of research into the areas of orthopedic biomaterial design, mechanical characterization of FFF parts, and lattice structures. The following chapters will further define the relationship between the current work and the respective topics of study. The sequence of this document will include a literature review, an overview of the experimental methods and objectives, the subsequent results, and the conclusions of this study and recommendations for further work.

CHAPTER TWO

LITERATURE REVIEW

Mechanical Characterization of FFF Components

As of the time of this publication, there remains a lack of standardized test methods for many aspects of AM- particularly FFF. To accommodate for this lack of guidance, studies typically rely on the nearest applicable test method as a substitute. The test methods most commonly relied on in these studies to characterize tensile properties are ASTM D638 [35], [40], [59], [81]–[86] and ISO 527 [45], [87]–[90], both utilizing a dogbone style specimen. Using the same methods to characterize 3D-printed parts as solid molded polymer specimens (e.g., injection molded) is likely insufficient for proper characterization [91]. Protolabs- a low volume digital manufacturing company- uses ASTM D638 for tensile testing of 3D-printed plastics [92]. They do, however, acknowledge the impact of the printing process and parameters on part quality and report the direction of testing relative to build orientation.

Park et al. (2020) attempts to highlight some critical drawbacks which can be seen when using D638 to characterize AM parts [40]. The reported results show a large variation of data, and higher likelihood of an undesirable failure outside of the gauge region of the specimen. The scattered results seen are believed to be due to inherent porosity and surface features inherent to FFF, both of which act as a stress concentrator and typically leads to premature failure. Due to these slight variations of cross-sectional area (CSA) relative to the filament layers and any defects, concerns over calculation

accuracy are also expressed. Both the tensile strength and variability were shown to be improved when the specimen surfaces were machined prior to testing.

Hyatt et al. (2020) presents a similar topic in which FFF-printed Ultem 9085 is characterized using the standards most commonly relied on for AM polymers [93]. ASTM D638 was used for tensile testing, however, the original Type I geometry used experienced a high incidence level of premature failures at the fillet due to stress concentrations. To address this, the tensile coupon was redesigned to remove the sharp corners at the transition between the tab and filleted edge. The smoother "streamline" design resulted in more favorable failures and an increase in tensile strength. The authors additionally expressed concerns of the part stability when printing specimens vertically and explored alternative test methods to address this. Printing vertically is additionally known to significantly increase print time, relative to the XY axes.

American Society for Testing and Materials (ASTM) Standardization of Additive Manufacturing

ASTM formed Committee F42 in 2009 to cover AM technologies [94]. This committee is comprised of 22 subcommittees covering an array of topics including test methods, the different material classes used (i.e., metals, ceramics, and polymers), and various relevant industries (e.g., aerospace, medical, construction) [95]. Since the formation of this committee, several standards have been released, however they are predominantly dedicated to metal powder-bed printing. While this is an apparent decision driven by which forms of AM are of particular industry interest, there remains a lack of guidance for polymeric components fabricated via FFF.

It was announced in the beginning of 2022 that the F42 Committee approved a new guide for “layer-based material extrusion processes” in AM [96]. Until that guide is released, the only relevant active standards mostly seek to standardize the terminology used [97], [98], data processing involved [99], and the information and format of any reporting [100]. The most involved of these FFF-specific standards is a two-part guide on material-extrusion based AM of polymers, covered in ASTM 52903-1 and 52903-2 [101], [102]. The first part of this guide specifies the feedstock requirements, while the latter outlines a framework to instruct the fabrication and testing of FFF specimens, however, the guidance is not as thorough as many other ASTM test methods. For example, the instruction to report key processing parameters (e.g., print speed, nozzle diameter) outlined in this standard is beneficial, but there is no specification on many design aspects, leaving the method fairly open-ended. Current methods are mostly sufficient to validate many printed components, but what is needed are standardized methods to characterize FFF-specific properties to improve repeatability. Given the pronounced anisotropic nature of FFF parts, ILA has the potential to be an effective characterize metric for parameter optimization.

FFF Parameter Optimization for Mechanical Characterization

While FFF has not seen the same prevalence in manufacturing as other additive methods, it has remained firmly established for research and prototyping applications. There have been numerous studies detailing the efforts to characterize the mechanical properties of FFF parts, despite a lack of any standardized test methods for this

manufacturing method. Without having any specific guidance for this purpose, the resulting studies can vary considerably in methodology [35].

The review published by Gordelier et al. (2019) covers many topics of concern for the present study as they relate to AM mechanical characterization and parameter optimization [55]. The authors highlight the lack of AM-specific test standards, and the large variation of the measured properties as a result. Concerns about the typical dogbone geometry causing premature failure at the fillet are also noted, similar to those found in Hyatt et al. (2020). Several other studies were reviewed in which print parameters were optimized to maximize tensile strength to attempt to identify any important trends. Most notable of these results is the majority finding of peak tensile strength with a layer orientation parallel to loading, and a layer height of 0.2mm. It is worth mentioning, however, of the studies which determined 0.2mm to be the optimal value, the range of heights included in these studies were limited to the range of 0.2mm to 0.4mm. The other studies investigated a smaller range of 0.6mm to 0.24 mm and found the results to be generally unclear.

Abidin et al. (2021) covers another study which attempts to optimize the FFF parameters for the purpose of tuning the porosity of a PLA scaffold [103]. The influence of temperature, print speed, and layer thickness were evaluated using the Taguchi method to reduce the required number of trials. The results of this study showed nozzle temperature to be the most significant influencing factor, followed by layer height, print speed.

PEEK can be 3D-printed without affecting biocompatibility, allowing for patient-specific implants to be produced [104], [105]. Steinberg et al. (2013) investigates the biomechanical properties and debris generation of select CF-PEEK orthopedic implants [106]. The composite implants were found to have reduced particle generation and sufficient mechanical properties to serve as a viable alternative to the existing metallic implants being compared. As the author states, CFR-PEEK composites "show a high utilization of the fiber in stiffness and strength, and a similarly high utilization of the matrix ductility in toughness" [106]. More comprehensive reviews of the performance of PEEK and CFR-PEEK for orthopedic applications have been conducted and can be found elsewhere [33], [107], [108].

Xiaoyong et al. (2017) investigated the impact of extrusion and chamber temperature on the properties of 3D-printed PEEK [90]. This study is one such example in which a specimen geometry similar to D638 is used, and the filament orientation of the infill is 45° with respect to the axis of loading. For the purpose of a direct comparison, however, the authors were able to observe the significant impact the thermal processing parameters had on the resultant tensile strength. The authors identify the mechanism of this improvement as an increase in the bonding forces of the specimen.

Interlayer Adhesion (ILA) Optimization Studies

Parameter optimization of 3D-printed PEEK for the purpose of improved layer adhesion has been increasingly studied. The semi-crystalline nature of PEEK increases the sensitivity to changes in processing parameters, making it a beneficial material for this work [109]. Liaw et al. (2021) conducted one such study investigating the ILA of

PEEK specimens [32]. The adhesion force was characterized via flexural testing of a hollow, vertically printed rectangular specimen. The variables included in this study were extrusion temperature, print speed, layer height, and “wait-time” between layers. The authors used a design of experiments (DOE) approach in order to efficiently evaluate these parameters without adding a significant number of additional trials. The results of this study found the nozzle temperature to be the most influential factor, followed by wait-time and layer heights, while print speed was not found to be as significant. Reduced layer heights were additionally found to be correlated with an increase of the modulus. The authors propose the described characterization method they used as a viable procedure to measure the ILA of 3D-printed PEEK.

Rodzeń et al (2021) evaluated the effect of the chamber temperature on the resultant ILA of FFF-printed CFR-PEEK [110]. The specimens were prepared by printing out what the authors refer to as a “wall” structure and extracting samples according to ASTM D638 Type V via water jet. The results presented show a reduced thermal gradient of the structure and increased tensile strength and crystallinity when increasing the chamber temperature from 78°C to 230°C. The optimal results of this work occurred at a build plate and chamber temperature 240°C and 230°C respectively. These temperatures support previous findings that the crystallization rate of PEEK is expected to be greatest around a temperature of 230°C [111]. The authors also noted the critical distinction that since any reinforcing fibers generally to align with the polymer flow, they have little to no impact on the observed bonding between layers.

Overmolded Lattice Structures

At the time of writing, there are no other literature known which investigate FFF-printed lattice structures as a reinforcing component of an overmolded composite. The most applicable comparisons in the literature that can be found primarily utilize the lattice structures as a multi-material joining method, due to the increased interfacial bonding. The work published in Ryan (2020) investigates the use of FFF-printed PLA lattices, overmolded with silicone, can improve the interfacial strength [112]. The printed architectures included body-centered cubic, octet, and gyroid lattices. The use of these lattices showed promising results for their use in joining applications, however, the disparity of mechanical properties between the printed structures and the silicone prevented the mechanics of the lattices to have a significant role. The most similar published work was found in Verma et al. (2022), in which three lattices 316L stainless steel were 3D-printed via SLM and overmolded with polyaryletherketone (PAEK) [113]. The purpose of this work is similarly to maximize the interfacial strength between the metal substrate and injection molded polymer.

CHAPTER THREE

MATERIALS AND METHODS

This work herein proposes a novel composite structure in which an FFF-printed gyroid lattice is overmolded with a weaker polymer. The purpose of this composite is to improve the strength and energy absorption of the overmolding resin. To maintain applicability to BTE, the material selection and design was limited to those which could be utilized in the field. The overmolding polymer chosen was Ingeo™ 4043D PLA (NatureWorks) and the printed gyroid lattices were printed using CarbonX™ CFR-PEEK filament (3DXTech) [114], [115]. The experimental procedure consisted of two phases. The first phase was the optimization of the FFF parameters as it relates to the measured ILA force, followed by the manufacturing and characterization of the overmolded lattice (OML) composite.

All mechanical characterization was performed on a Test Resources 313 Series universal test frame with a load capacity of 50 kN. All test specimens were conditioned prior to testing according to ASTM D618-21 Procedure A [116]. All FFF components were printed with an Intamsys Funmat HT Enhanced using a 0.4mm diameter hardened steel nozzle.

Optimization of FFF Printing

Prior to printing any lattice components, the parameters were optimized in order to maximize performance of the composite and attempt to minimize any defects or failures due to improper processing parameters. Mechanical failure of FFF parts is most likely to occur due to delamination between the discrete filament layers along the Z-axis.

To evaluate and maximize this force, the layer orientation and mechanical characterization of the printed specimen must isolate the ILA. To test this bonding force, it was decided to conduct tensile testing on vertically printed tensile specimens. Printing in this orientation results in a loading direction orthogonal to the filament orientation, guaranteeing the measured tensile force to be the quantification of the weakest ILA which could cause such a failure. For this purpose, unfilled ThermaX™ PEEK filament was used to ensure any observed improvement was solely due to improved bonding and crystallization of the polymer. The original test method used was according to ASTM D638-14, however, modifications to specimen design and test procedures were modified as needed. The objectives of this phase are (1) design optimization with respect to vertical print stability and minimization of improper specimen failure, and (2) parameter optimization to characterize the influence of key printing parameters on the measured ILA.

To properly isolate and quantify the ILA, it is crucial that the specimen orientation was aligned as accurately as possible. If the specimen is placed at an angle, the load will be partially transferred along the filament layer, skewing the results. To improve the accuracy of specimen placement, and minimize human error, an alignment jig was designed and printed to ensure consistent placement and orientation of the specimen between trials. An illustration of the jig design used is provided in Fig. 3.1, as well as in position to demonstrate its use.

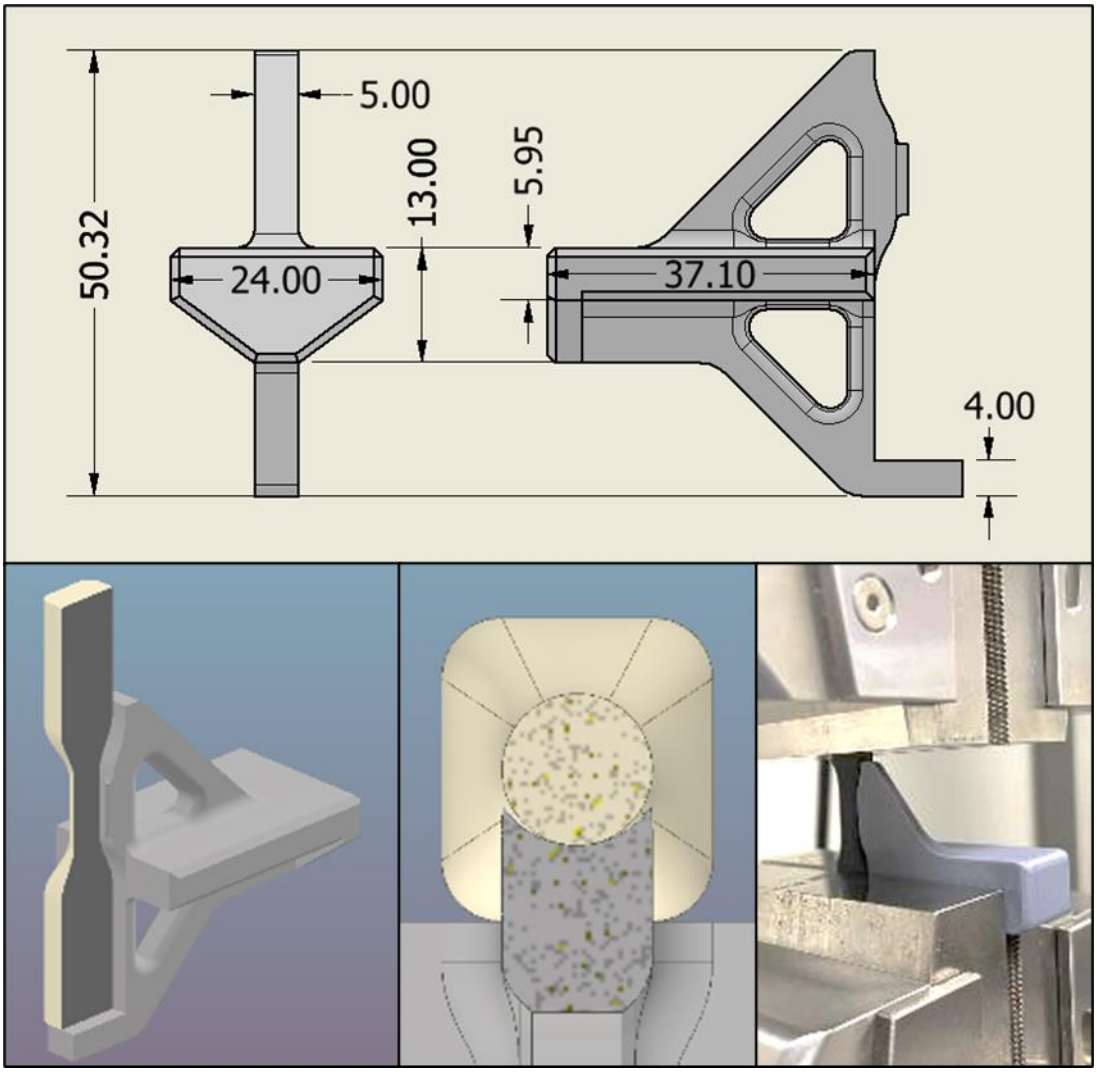

Figure 3.1 – Alignment jig design drawing images with dimensions in mm (top), CAD model with cross-section of ILA dogbone in place (bottom left), top view showing the cylindrical fit of gauge section (bottom center), and jig in place on tensile wedge clamps (bottom right). The jig included in the last image shows the equivalent design produced for the modified Type V specimens.

Design Optimization

As mentioned in previous sections, FFF-printed specimens are generally not printed vertically out of concerns for instability and significantly increased print duration. Despite these concerns, vertically printed specimens ensure the proper layer orientation for ILA characterization. The original specimen used was ASTM D638 Type V, due to the small specimen size in order to minimize both of the mentioned concerns. To further stabilize the model during printing, the specimens were printed either 6 or 12 at a time, with bridging members added between the specimens, and printed with a brim to increase adhesion to the print bed. The bridging members were modeled as rectangular beams between the vertical specimens. An illustration of these stability enhancements is included in Fig. 3.2. The size and the location of the bridging members shown in this figure represents those used in the final version of the proposed ILA specimen used to optimize the printing parameters. Changes to the printed model were evaluated based on qualitative observations during the printing process and while handling, as well as their quantitative impact on ILA data.

All specimens prior to the parameter optimization study were printed with a layer height and print speed of 0.2mm and 60mm/s, respectively. The range of extrusion temperatures used was 400-450°C, to verify any adverse effects were not due to insufficient thermal conditions. The original intent was to increase extrusion temperature until the ILA properties or general printability is adversely affected. This was not the behavior seen, however, as neither the properties nor general printability suffered prior to reaching the maximum printing temperature of 450°C. Any modifications made to the

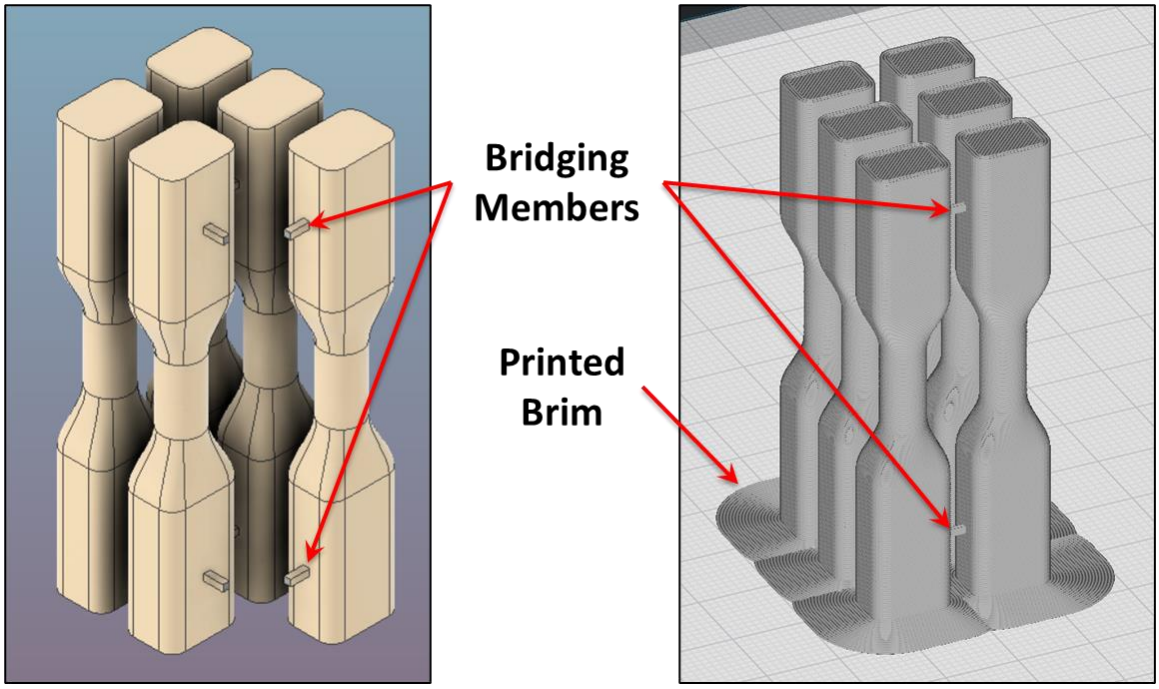

Figure 3.2 – Methods used to improve vertical print stability. The printed brim increases the surface of the first layer and resists delamination. The bridging members provide structural support to resist translational motion introduced by the motion of the print head. The width and depth of each specimen are 10.8mm and 8mm respectively, with 3mm spacing between all specimens in the printed model. The height of the printed model is 63.5mm, matching that of the original Type V geometry. Bridging members are modeled as 1mm-by-1mm rectangles with a center distance of 8.5mm from each end of the specimen.

specimen design were based on the defects, improper failure modes observed, or general incompatibility with the FFF process and ILA testing. For this work, improper failure primarily refers to a delamination failure sufficiently outside of the desired gauge region. The evolution of the specimen design and their respective specifications are presented in Fig. 3.3 and Table 3.1, respectively. This ILA study incorporated two modified iterations of the original Type V tensile specimen. The reasoning for any modifications and the comparison between the design iterations are included in the next chapter.

Parameter Optimization

Once the redesigned specimen geometry was established, a DOE study was conducted in order to observe the influence of these variables on ILA. This method was selected to significantly reduce the required number of trials compared to following an iterative process for each variable. The parameters selected to study included extrusion temperature (400°C-450°C), print speed (30mm/s-60mm/s), and layer height (0.1mm-0.3mm). The DOE study and subsequent statistical analysis was performed using JMP Pro 16.0.0 and included 16 trials. The generated parameter combinations for each trial can be found in Table 3.2.

Lattice Design and Overmolding

The design criteria for the lattice included printability, ease of overmolding, and the potential for tissue integration *in vivo*. The lattice should additionally provide improved stiffness and energy absorption to the composite. The morphological requirements for both overmolding and tissue integration translate to the need for an open

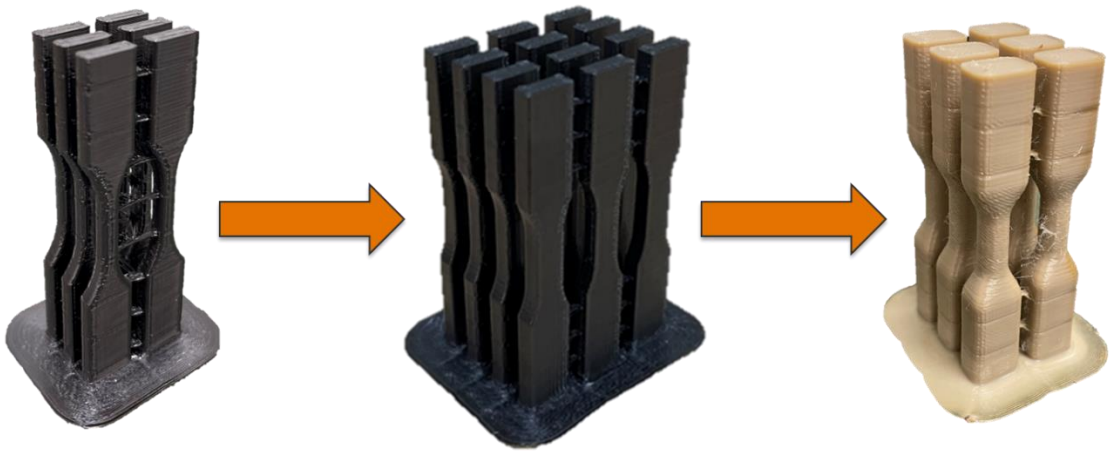

Figure 3.3 – Visual evolution of tensile specimen design. ASTM D638 Type V (left), modified Type V (middle), and the final proposed ILA dogbone design (right). The modified Type V design print batch was increased to 12 based on the increase of improper failures and variation seen in the ILA results.

Table 3.1 – ASTM D638 Type V Design Modification

*Aspect Ratio refers to the ratio of the cross-sectional area (CSA) of the tab to the gauge region

Dimensions (mm)	Type V	Modified Type V	ILA Specimen
Tab Thickness	3.2	4	8
Tab Width	9.53	9.53	10.8
Gauge Width	3.18	6	
Gauge Diameter			6
Length of Narrow Section	9.53	9.53	10
Gauge Length	7.62	7.62	8
Tab Fillet Radius	N/A	N/A	2
Length	63.5		
Aspect Ratio*	2.997	1.588	2.934

Table 3.2 – DOE Study Trial Parameters.

Trial	Print Temperature (°C)	Print Speed (mm/sec)	Layer Height (mm)
1	425	45	0.2
2	400	60	0.3
3	450	30	0.1
4	400	30	0.1
5	425	45	0.1
6	450	30	0.3
7	425	60	0.2
8	450	45	0.2
9	400	45	0.2
10	400	60	0.1
11	400	30	0.3
12	450	60	0.3
13	425	45	0.3
14	450	60	0.1
15	425	45	0.2
16	425	30	0.2

interconnected porous structure. Such a morphology is necessary to allow for both the polymer flow during overmolding as well as cell mobility in TE applications.

All design and evaluation of any lattice structures was performed using nTopology 3.17.4. Only periodic structures were considered for use to allow for improved predictability in the composite mechanics. Plate lattices were also excluded due to their lack of cell interconnectivity. Minimal CSA variance was selected as the determining factor in order to maximize the properties of for any lattice which meets all the above requirements. For this reason, two TPMS lattices- gyroid and diamond- were considered which have very low values of CSA variance. To validate any selection, the relative CSA for of these lattices were compared with the other TPMS options on nTopology, and the IsoTruss for reference. To compare the CSA of the selected lattice structures, the same 40mm cube volume was used to generate all the lattices. the TPMS bodies all had a unit cell size of 8mm while the IsoTruss was normalized to the mass of the gyroid and diamond lattices. The CSA measurements were taken at 0.5mm increments throughout one cell length. The comparison of these measurement can be found in the next chapter.

Three-point bend testing according to ASTM D790-17 was the chosen method to characterize the OML composite. All injection molding was performed on an APSX-PIM using the ASTM D790 mold purchased also from APSX [117]. The barrel temperature, mold temperature and injection pressure used was set at 215°C, 65°C and 21.5 MPa, respectively. These parameters were used to mold both neat PLA specimens and for lattice overmolding. The performance of the composite OML samples was compared

against the flexural properties of PLA, the CFR-PEEK gyroid lattice as-printed, and both PEEK and CFR-PEEK printed at 100% infill. The results for each of these materials were normalized according to specimen density to effectively compare the properties.

Data Analysis

While efforts were taken to reduce the number of trials, the data collected in this study includes over 200 tensile tests, and about 50 flexural trials. In order to effectively analyze and compare all the data, two Matlab scripts were written to streamline this process. The first file produced was used to convert the text of the G-code files into a series of time values mentioned after each printed layer throughout the print process. This G-code analysis script was used to monitor the fluctuations in layer time throughout the prints. The time values were plotted against the completion percentage of each print to normalize the X-axis to allow printed models and parameters to be compared regardless of differing numbers of layers.

The main function of the second script is to extract and plot the trial data and provide the desired values. The results of the ILA study relied solely on the generated load-displacement data. The purpose of this was to avoid any potential calculation errors due to the slight CSA variation as a result of FFF layer discretization. The load drop threshold was set at 25% for the analysis of the ILA data, but that value for flexural trials was increased to 80%. The primary metrics of interest for all of the tensile data is determining the ILA (i.e., maximum load), and energy absorption. Examples of the graphs generated from both Matlab scripts are shown in Fig. 3.4.

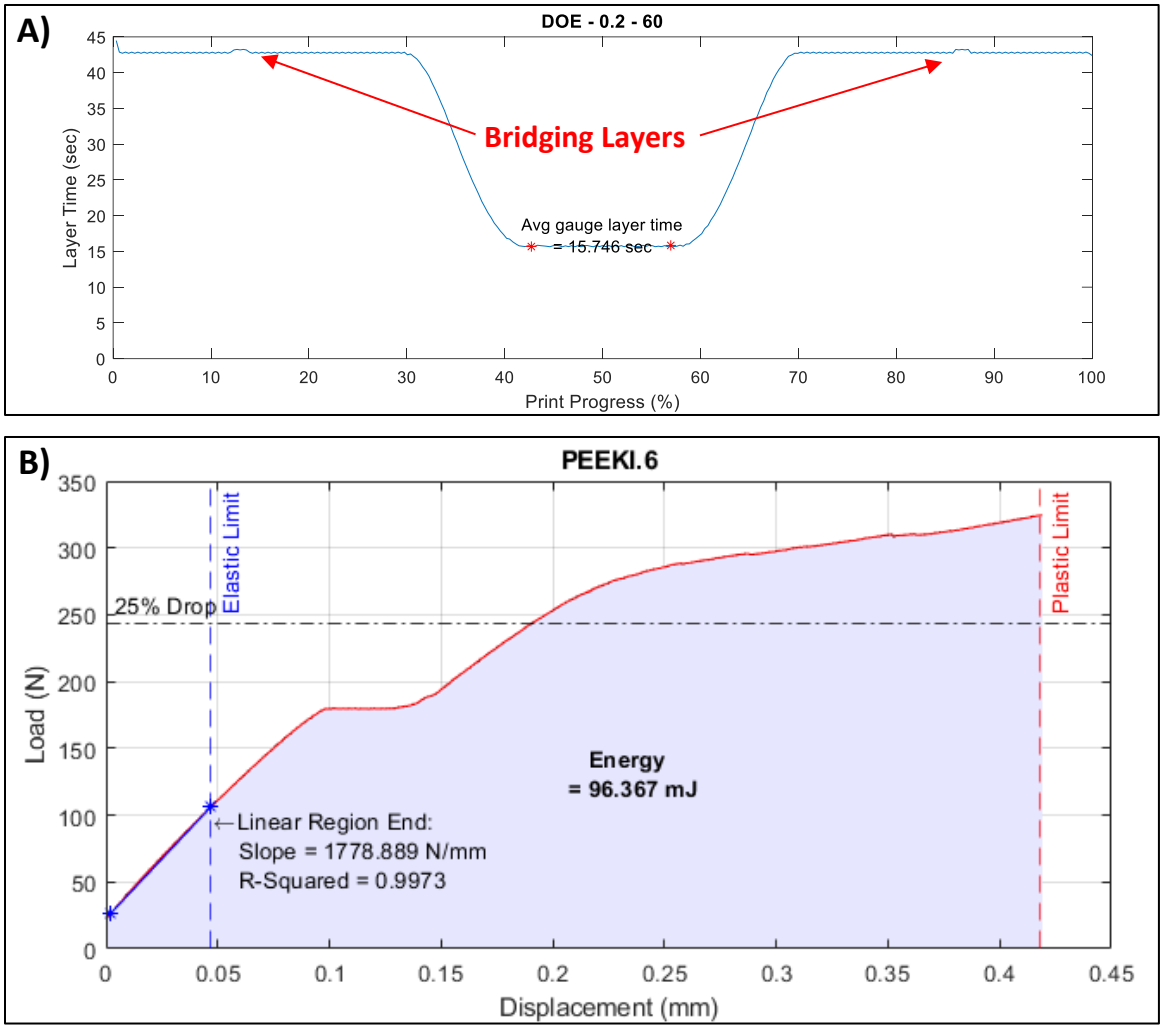

Figure 3.4 – Examples of Matlab generated graphs used for this work. A) Top graph shows the reported layer times for a print batch of ILA specimens printed at 60mm/s and 0.2mm layer height. The bridging architecture is reduced to 2 connections in this example, which can be seen as slight increases in layer time. An interesting phenomenon is the resemblance of these time curves to the profile of the specimens being printed. The data shown in the bottom graph B) corresponds to modified Type V specimen printed at 450°C.

CHAPTER FOUR

RESULTS AND DISCUSSION

FFF Optimization

The optimization results of the FFF process confirms findings found in the literature and identifies the area which deserve further investigation. As for specimen design, the defects and premature failure commonly seen can be attributed to the use of a specimen geometry which is not optimized for FFF. Increasing the aspect ratio of the specimen and eliminating any sharp edges resulted in more reliable tensile performance. The parameter optimization identified extrusion temperature as the most influential factor on ILA, reaffirmed what many other studies have shown. In general, increased extrusion temperatures and print speeds and decreased layer heights are correlated with overall strength improvements of FFF-printed components.

Model Stability and Design Optimization

The modifications made to the printed model was found to be a reliable method to maintain stability during printing. While adding a brim to FFF parts is not innovative by any means, none of the tensile model prints failed due to delamination from the print bed. The bridging members also were effective in eliminating any translational motion from the print head, however, the original architecture needed to be modified to not introduce defects into the gauge region of the specimen. The original model can be seen in Fig. 4.1, as well as the evolution of the bridging architecture. It was quickly seen that the layers where these connections occurred adversely affected the ILA at this point. This is assumed to be due to a reduction in polymer crystallinity as a result of increased cooling

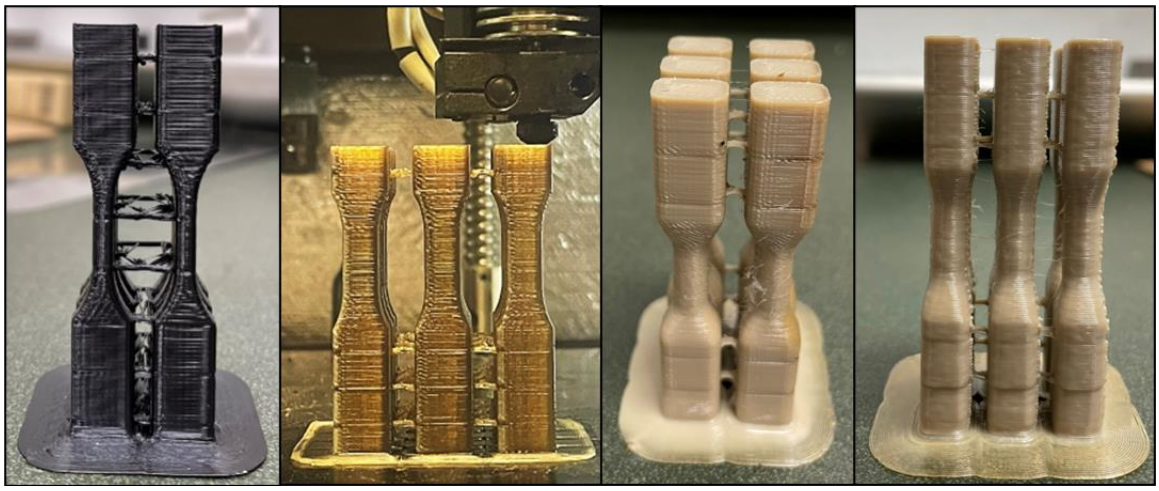

Figure 4.1 – Different iterations of bridging members of specimen design. The images (from left to right) include the Type V model with 8 equidistant connection points, which was then reduced to 6 connections limited to the tabs of the modified Type V model. This was again reduced to 4 connections for the ILA dogbone seen in the last two images.

time between the printed layers.

It should be noted that for the Type V and the first modified iteration, these connectors only attached on the side of the specimens which would not be in contact with the clamping surface. The intent of this was to avoid any sanding or filing which could damage the specimen or otherwise alter the filament surface of the gauge length. This connection architecture was not well-optimized, however, and resulted in longer layer times than necessary, and overall poor print accuracy. The thicker tab design of the ILA dogbone allowed any tab face to be sanded without contacting the gauge region. This enabled the redesign of this connection architecture seen in the last image of Fig. 4.1. This new architecture was able to use less material and follow a more efficient toolpath. Both of these factors decreased the additional layer time while printing the bridging members. Consequently, the effect of the crystallinity-induced defects seen at these layers is further minimized. The comparative improvement of layer time addition at the bridging layers is presented in Fig. 4.2. Layer times were extracted from the G-code files used and normalized for comparison. This normalization included isolating the local peak behavior and subtracting the values relative to the average layer times of the tabs before and after. The same range of 15 data points was used for both architectures and plotted against each other for direct comparison. The maximum layer time addition reduced from 6.94 sec to 2.34 sec as a result of this new design. While the effect on crystallinity was still present, its impact was significantly reduced.

The Type V specimens were very fragile and frequently broke while removing and handling the parts. Additional concerns arose while attempting to test the specimens.

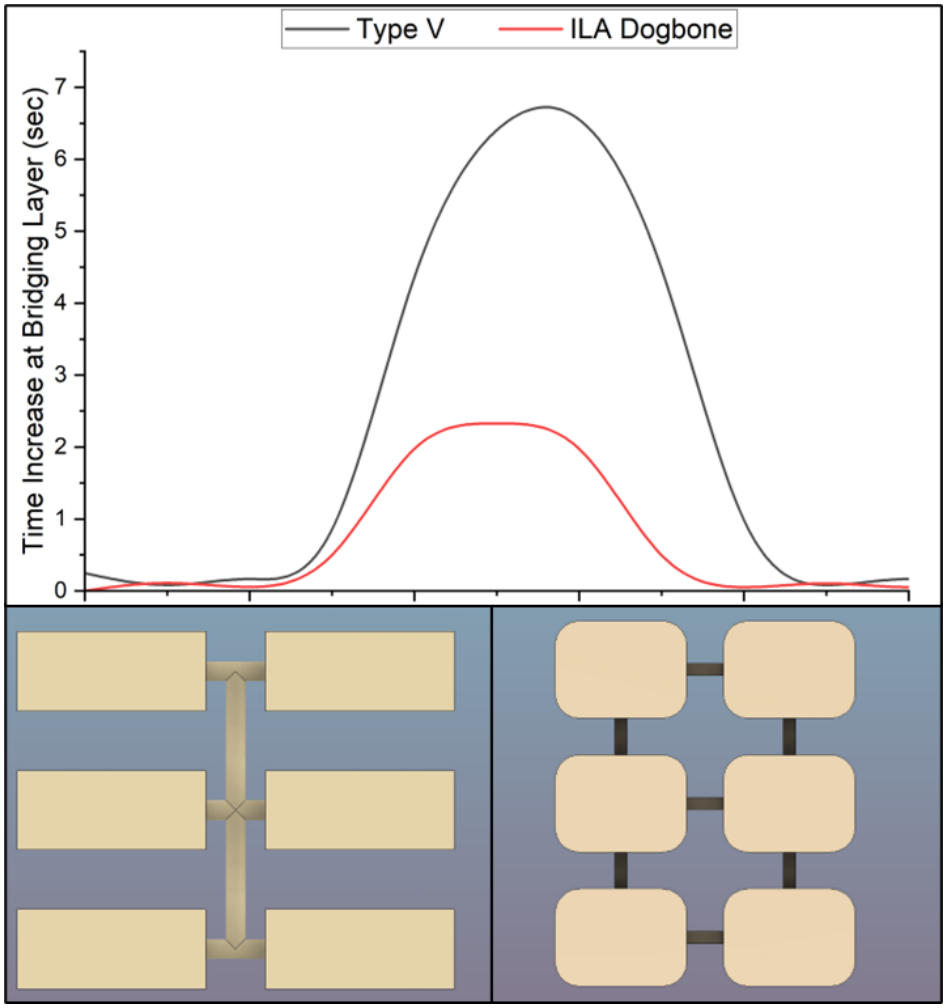

Figure 4.2 – Reduced addition of layer time at the bridging layers as a result of the new bridging architecture. Images show the comparison of the original bridging architecture (left) and the redesigned version (right). The X-axis is based on the arbitrary range of 7 data points before and after the local peak for each architecture. The increase in time is relative to the steady-state layer time of the tabs before and after this peak.

The tensile clamps used for tensile testing allowed for a small degree of rotation, which introduced damage to several parts prior to testing. For those which were not damaged, the tests at the minimum recommended speed of 1mm/min resulted in very rapid failures. No useful comparisons could be made with this data.

To address the issues experience with the Type V specimens, the next design iteration included modified bridging connectors and increased CSA. Additionally, the testing speed was reduced to 0.1mm/min to introduce a gradual failure. The bridging layers were limited to the tabs to ensure consistency throughout the gauge layers. The increase of both depth and gauge width improved the general durability of the printed specimens. Undesirable failure modes similar to those described in the literature were observed in this modified Type V design, however, the slower test speed did produce a more desirable data curve. During the brief thermal study using this specimen geometry, increases in extrusion temperature were correlated to an increase in the measured ILA values as expected. The adhesion force for each temperature set- illustrated in Fig. 4.3- shows a direct relationship between the extrusion temperature of the polymer and the average ILA force. This relationship is clearly apparent amongst the data, however, of the 104 trials, only 20 (19.2%) of those trials failed with the gauge length of 7.62mm.

The third iteration of the specimen design was intended to maintain the durability provided by the modified Type V, while improving the likelihood of desirable failures withing the gauge region. The design of the ILA dogbone incorporated the suggestions outlined in Park et al. (2020) and Hyatt et al. (2020)- increase the aspect ratio between

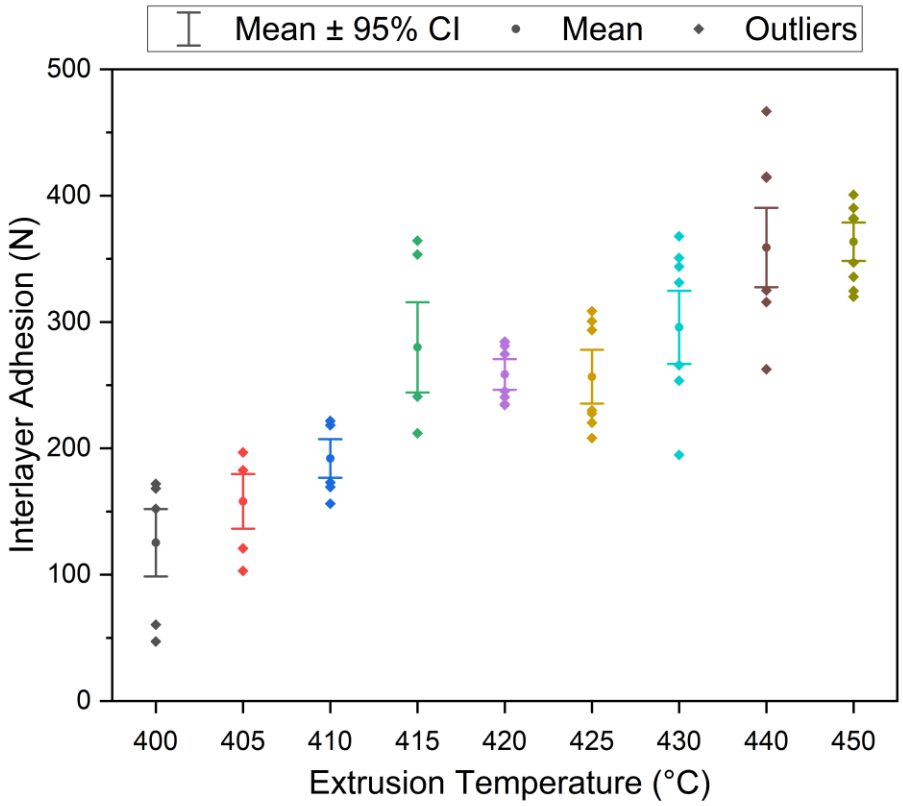

Figure 4.3 – Average ILA force of modified Type V specimens printed at 400-450°C. These results show the clear relationship between the printing temperature and the measured layer adhesion, but also with a large variation in the data.

gauge and tab area, and remove sharp edges [40], [93]. The latter suggestion was expanded to also incorporate a cylindrical gauge length. The purposes of this included improved printability and dimensional accuracy, as well as providing a more consistent layer path to reduce any potential variations of nozzle speed or material flow. The larger tabs of the ILA dogbone increased the aspect ratio to 2.934, compared to 2.997 for the original Type V specimen. This proposed design still experienced some of the same undesirable failures, but at a lower frequency than the modified Type V. The failure locations relative to the midpoint of both the modified Type V and ILA dogbone were measured to compare the rate of desired failures of both geometries. These results are represented by separate histograms for each specimen found in Fig. 4.4. Transitioning to the novel ILA dogbone design, the average failure distance from the midpoint was reduced from 6.11 mm to 4.81mm. The standard deviation was also reduced from 3.09mm to 2.18mm in the case of the ILA specimen. From this data, it can be seen that the failure of the ILA dogbone was more consistent, with a higher likelihood to fail within the gauge region.

DOE Study Results

The results of the tensile DOE study confirmed the findings both found in the literature, and the results of the previous thermal study. The printing temperature was found to have the biggest impact on both ILA and energy absorption. This was followed by print speed and then by layer height with a significantly reduced impact, but none other than temperature exceed the level of significance. The actual by predicted plots for ILA and energy absorption and parameter effect summary are included in Fig. 4.5. The

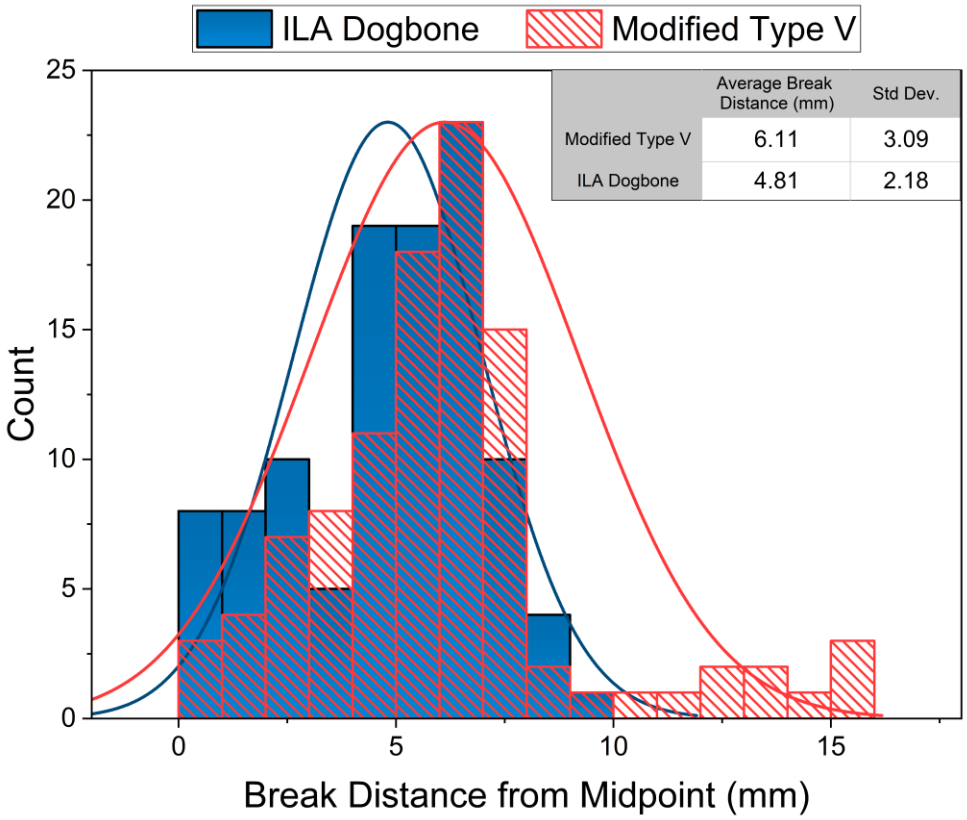

Figure 4.4 –Histogram comparison for the ILA dogbone design compared to the modified Type V. The leftward shift of the distribution curve, as well as the lower average and standard deviation values indicate more reliable failure modes with the use of the ILA dogbone specimen.

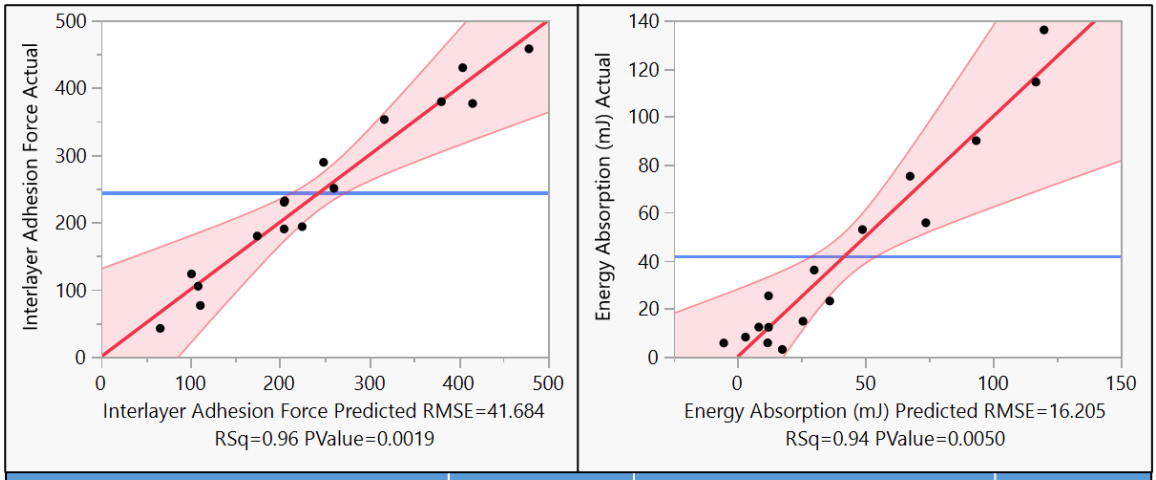

Source	LogWorth	PValue
Temperature(400,450)	4.314	0.00005
Print Speed(30,60)	1.760	0.01738
Layer Height*Print Speed	1.580	0.02630
Temperature*Layer Height	1.493	0.03215
Temperature* Temperature	1.157	0.06966
Layer Height*Layer Height	1.091	0.08117
Layer Height(0.1,0.3)	0.313	0.48653
Print Speed*Print Speed	0.197	0.63568
Temperature*Print Speed	0.134	0.73500

Figure 4.5 – DOE actual vs predicted plots for ILA and energy absorption results. The predictive models provide relatively accurate results, but the process needs to be further optimized to reduce variance.

predictive model ILA was slightly more accurate than that of the energy absorption, with R^2 values of 0.96 and 0.94 respectively. The ILA dogbone also experienced a large number of trials failing outside the desired gauge region, however, at a lower rate than previous. The ILA specimen had 31 acceptable failures out of 107 total trials, resulting in a 9.7% decrease in failures outside the gauge region. A simplified version of the DOE data grouped by extrusion temperature and print speed suggests the impact of print speed on ILA, despite not exceeding the threshold of significance for the generated predictive model. This trend of the average ILA data can be seen in Fig. 4.6.

From the collected data and that found in the literature, it was confidently confirmed that increasing print speed and extrusion temperature will result in an increased ILA force. The effect of layer height on layer ILA, however, seemed inconsistent and difficult to determine a trend. For example, comparing between trials of the DOE study which only differ in layer height, two of the four cases result in an increase in ILA due to reduced layer height, while the opposite is true for the remaining two comparisons. An additional round of testing was performed to determine whether a 0.1 or 0.3mm layer height would be superior. For this purpose, DOE trials 12 and 14 were repeated using CFR-PEEK filament. The data comparison for these trials is shown in Fig. 4.7.

As a result, the DOE-14 parameter combination (i.e., layer height of 0.1mm) was selected due to similar ILA in both unfilled and CFR-PEEK , and an increased energy absorption and displacement for CFR-PEEK specimens. Based on the observed data following the ILA characterization of both the modified Type V and the ILA dogbone,

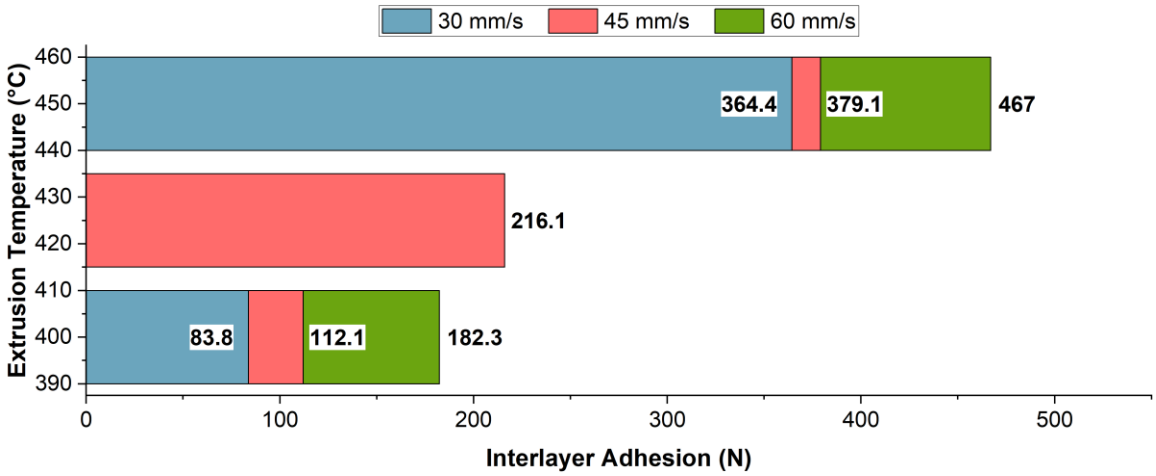

Figure 4.6 – Average ILA results from DOE study, grouped by temperature and print speed. The effect of increased print speed is seen to have a positive effect on ILA within the set optimization parameters.

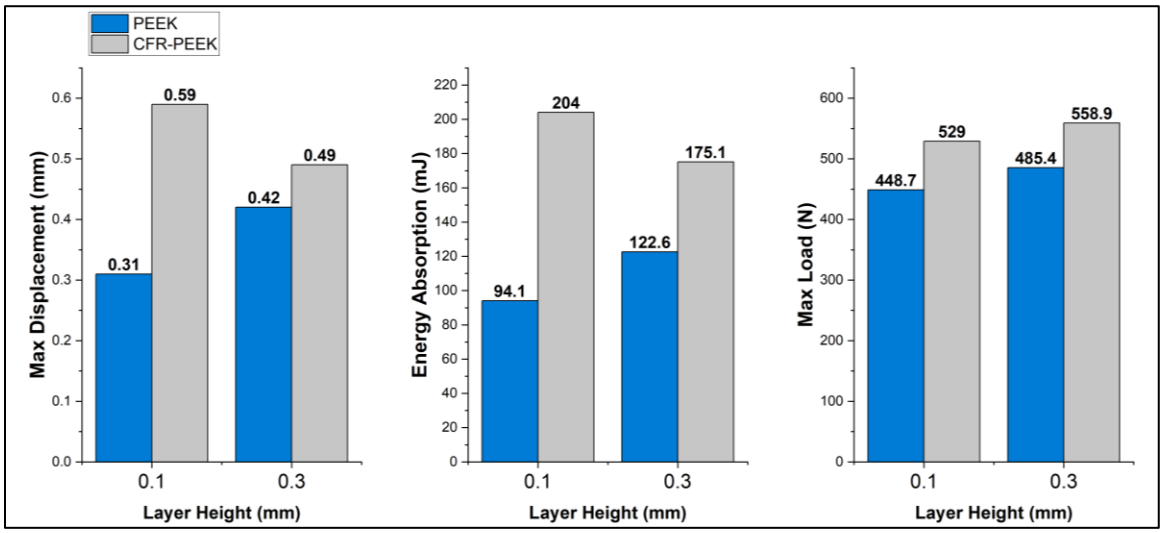

Figure 4.7 – Comparison of unfilled and CFR-PEEK ILA data and effect of layer heights according to DOE-12 and DOE-14 trial parameters.

the ideal parameter combination selected to print the gyroid lattice will include high print temperature, high speed, and low layer height. The temperature and layer height were maintained at 450°C and 0.1mm, respectively, but given the observed trend in the data, the print speed was increased to 80mm/s.

Overmolded Lattice Composite Results

Lattice Selection and Design

The CSA comparison of the selected lattices show both the diamond and gyroid lattices to be significantly more consistent in terms of CSA. The average relative CSA for the diamond and gyroid was 50% with standard deviations of 0.005% and 0.003% respectively. Given the negligible deviation in either case, no case can be made that one of these lattices would be superior, based on these CSA measurements. For practical purposes, however, based on these results, the gyroid lattice was selected. The data from these comparisons can be found in Fig. 4.8

The gyroid lattice was generated using the volume of the injection molded specimen to be tested. The width of the lattice volume was set to be 11.8mm, and the length was reduced by the same offset, resulting a length of 107.746mm. The lattice has a height of 3.5mm, greater than the dimensional thickness of 3.175mm on the injection molded design. The average depth, however, for the molded PLA specimens was measured to be 3.49mm, and this value was the basis for the depth of the gyroid. Illustrations of the lattice design and original flexural specimen are provided in Fig. 4.9. Also found in this figure is the tabulated specifications of the gyroid lattice. The unit cell of the gyroid lattice is not uniform in all directions, but instead normalized by the desired

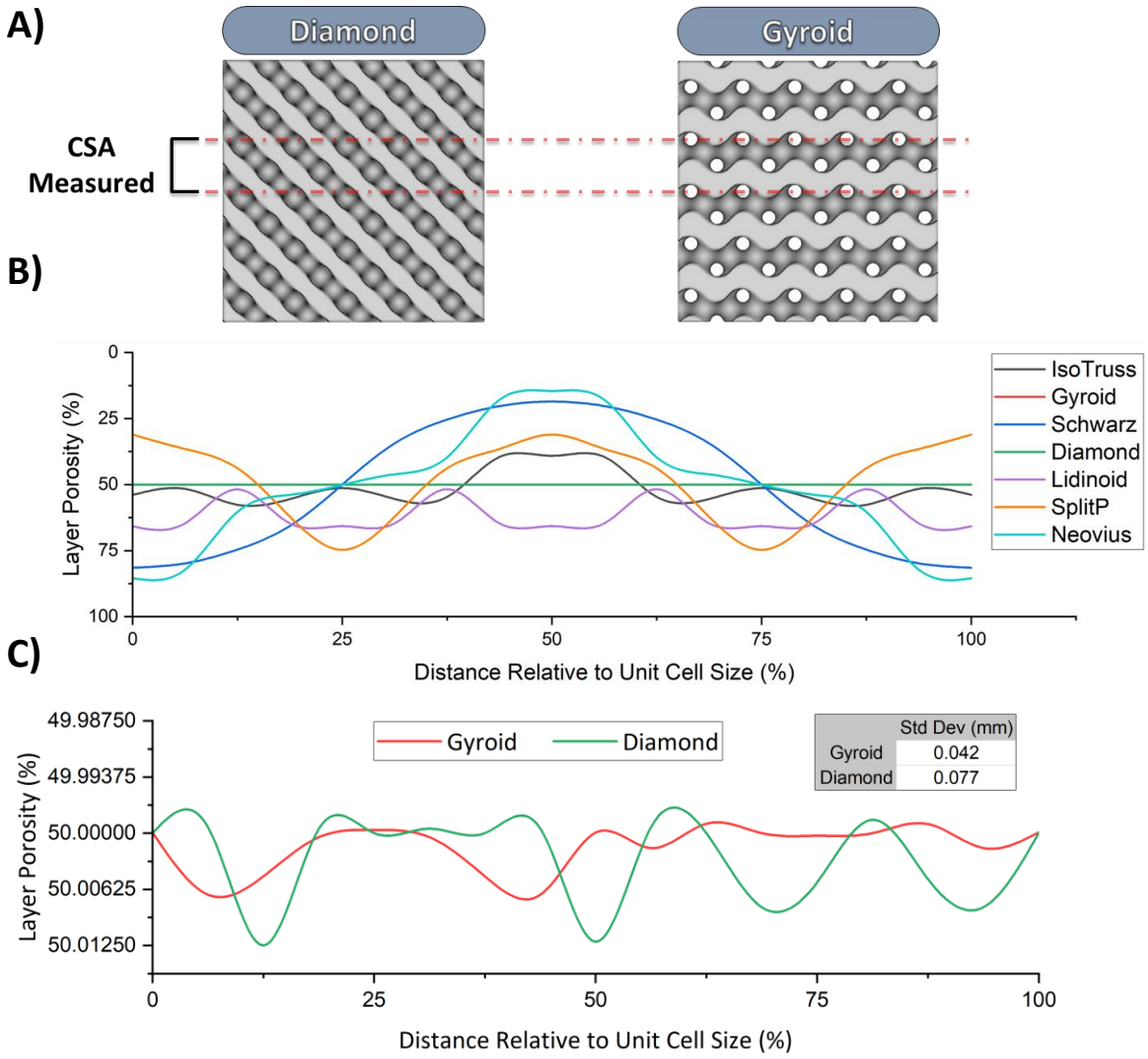

Figure 4.8 – Comparison of CSA throughout a single cell length relative to cell size. The 40mm lattice cube examples in A) show the diamond and gyroid as they were modeled for CSA measurement. The top graph in B) compare the CSA of several TPMS as well as the IsoTruss lattices. The gyroid line is not visible since the diamond and gyroid lattices both had volume fractions and standard deviations of 50% and <1% respectively. The individual comparison of gyroid and diamond is shown in C) and shows the gyroid to have the most consistent CSA.

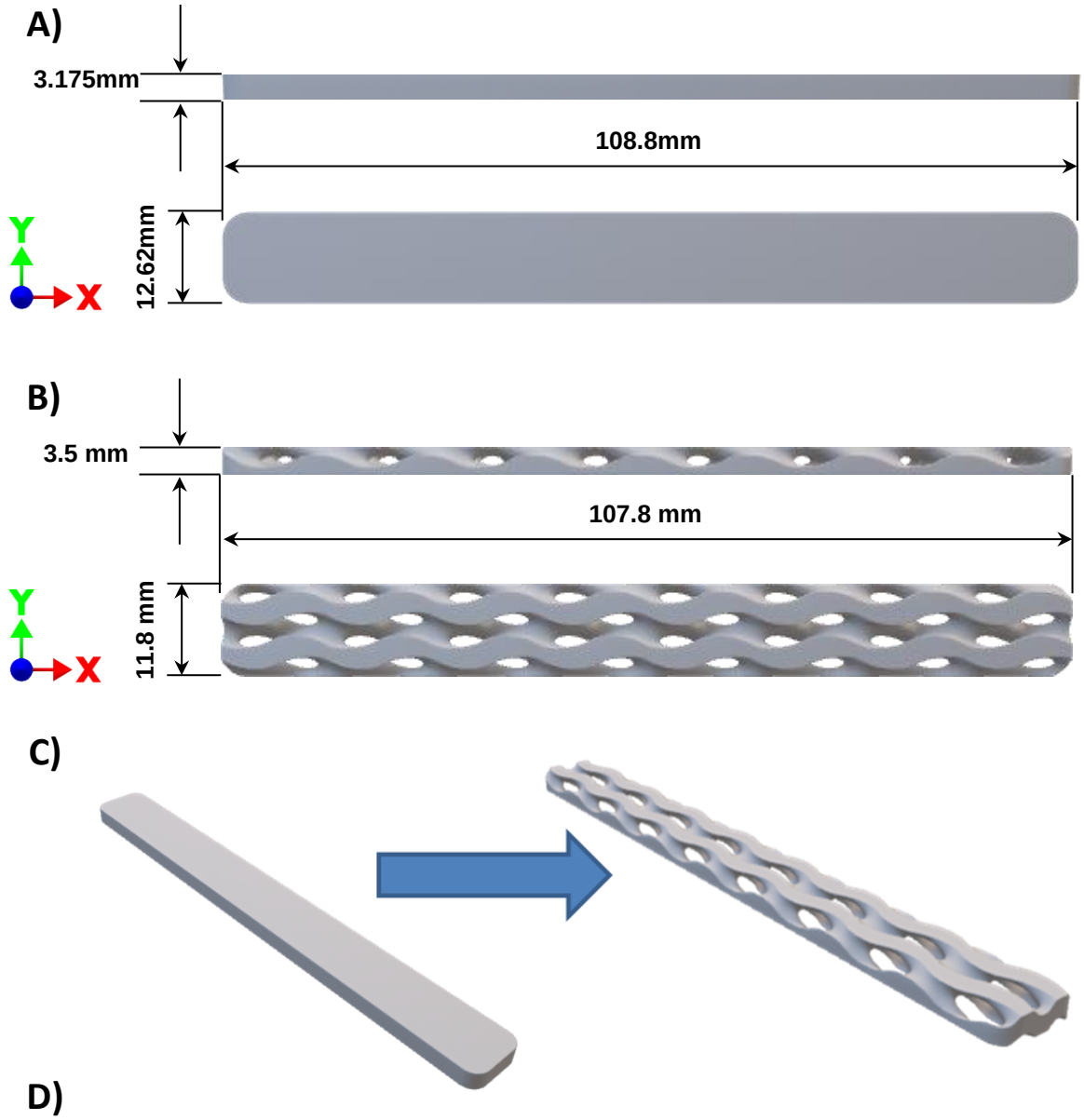

Axis	Cell Count	Cell Size (mm)	Print Parameters	Value
X	8	13.47	***Temperature (°C)***	450
Y	2.125	5.55	***Print Speed (mm/sec)***	80
Z	0.65	5.38	***Layer Height (mm)***	0.1

Figure 4.9 – Gyroid lattice design and specifications. The dimensional and visual comparison between the A) original injection molded volume, B) the offset lattice body, and C) the simplified process graphic showing the conversion the intended flexural specimen into the normalized gyroid lattice. The table in D) provides the non-homogenous unit cell size, and print parameters used to print lattice specimens.

number of cells in each axis. This non-uniformity serves to preserve the symmetry of the structure. Additionally, overmolding the lattice will include the polymer flow entering one end of the gyroid, and travel along the length of the lattice. For this reason, the increased cell size in the X-axis produces a desirable geometry to allow for polymer flow.

Flexural Results

The OML composite resulted in improvements in flexural strength, modulus, and energy absorption. The materials included the flexural characterization are injection molded PLA, the OML composite, CFR-PEEK gyroid lattice, and both PEEK and CFR-PEEK printed at 100% infill. All printed specimens were based off the injection molded volume, maintaining a constant specimen design throughout all trials. The results were normalized by density to include the improve comparison with the lattice specimens. The original and normalized data from all flexural trials are presented in Fig. 4.10. The densities of the PLA pellets, PEEK filament, and CFR-PEEK filament are 1.24g/cc, 1.3g/cc, and 1.39g/cc, respectively. The average density of the OML composite was found to be 1.298g/cc. The composite density of the OML was calculated using the measured masses of the composite and lattice samples, and the reported densities of the manufacturers. The formula used is presented in Eq 2, in which ρ and m refer to density and mass respectively.

$$\rho_{OML} = \frac{m_{OML}}{\left(\frac{\left(m_{OML}-m_{Gyr}\right)}{\rho_{PLA}}+\frac{m_{Gyr}}{\rho_{CFR-PEEK}}\right)} \quad (2)$$

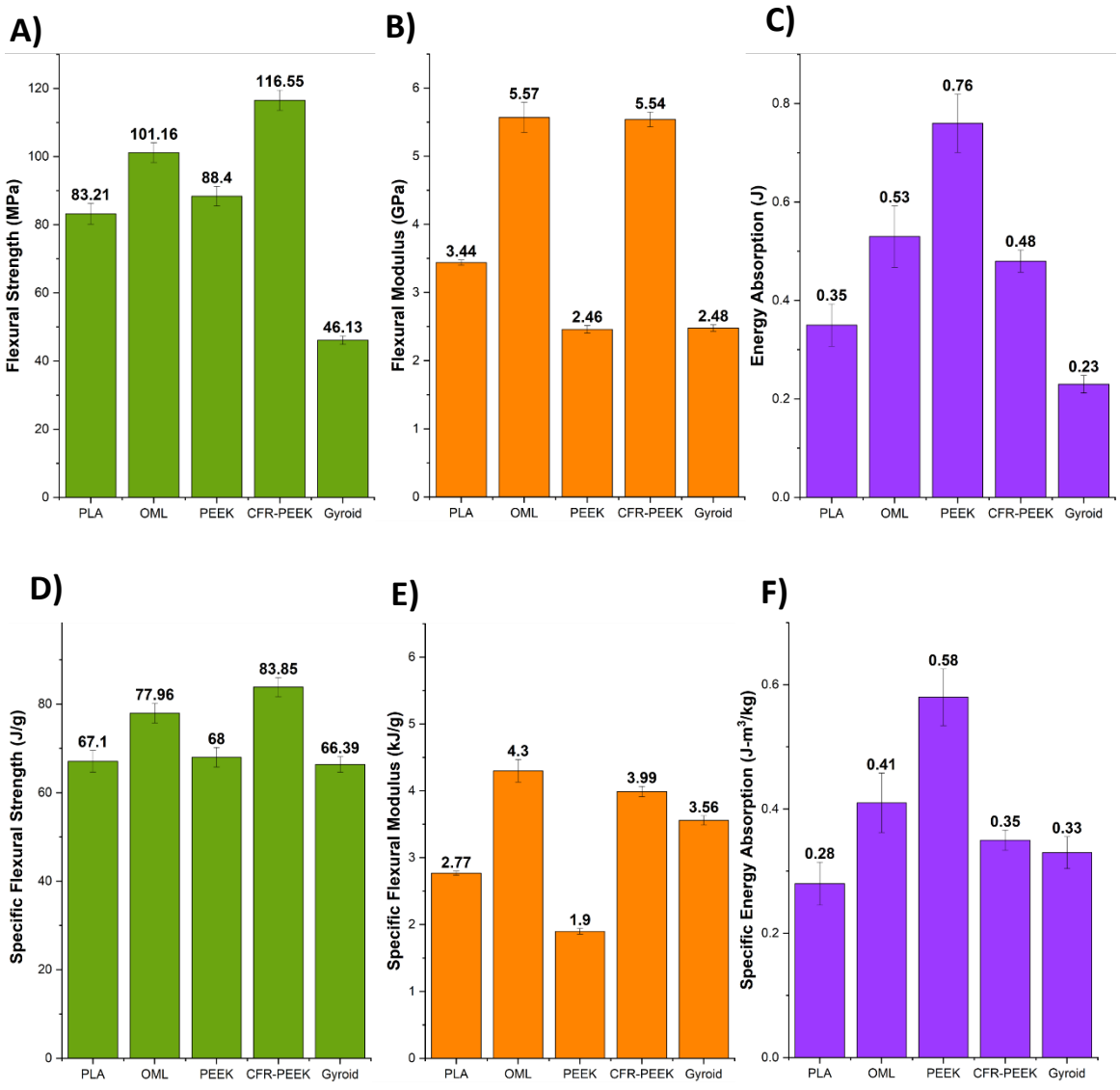

Figure 4.10 – Flexural characterization results. A) Flexural strength, B) flexural modulus, C) energy absorption, D) specific flexural strength (SFS), E) specific flexural modulus (SFM), and F) specific energy absorption (SEA). The OML composite showed properties superior to both of its constituents.

D)

The CFR-PEEK gyroid lattice was shown to have a specific flexural strength (SFS) similar to unfilled PEEK, and injection molded PLA. The lattice maintained a high specific flexural modulus (SFM) of 3.56GPa/g, which was 79.2% of the measured value for CFR-PEEK printed at 100% infill. The specific energy absorption (SEA) of the lattice was comparable to CFR-PEEK and 17.9% higher than that of PLA. The fracture behavior of the lattices followed a repeatable pattern, clearly indicating the failure point of the design. The fracture occurs along an axis between the locations of the smallest CSA near the midpoint of the lattice. The printed gyroid lattices and the observed failure path can be seen in Fig. 4.11.

The OML composite resulted in specific properties which exceeded that of both of its constituents. Overmolding the gyroid lattice resulted in SFS, SFM, and SEA improvements of 17.4%, 20.8%, and 24.2%, respectively. Similarly, the CFR-PEEK lattice reinforcement improved these properties of injection molded PLA by 16.2%, 55.2%, and 46.4%. The OML composite outperformed all other materials in terms of SFM. The SFM of the composite specimens exceeded that of both CFR-PEEK and unfilled PEEK by 7.5% and 225.8%. Unfilled PEEK provided the greatest SEA properties due to its improved ductility. This can be seen in Fig. 4.12, in which representative curves for PEEK, CFR-PEEK, and PLA are plotted for comparison. With the incorporation of CF, the average maximum displacement of PEEK during flexural testing was reduced from 7.68mm to 4.21mm, a 45.2% decrease. After PEEK, however, the SEA of the OML composite was greater than PLA, CFR-PEEK, and the gyroid lattice. The overmolded specimens and the fracture surface of one example are presented

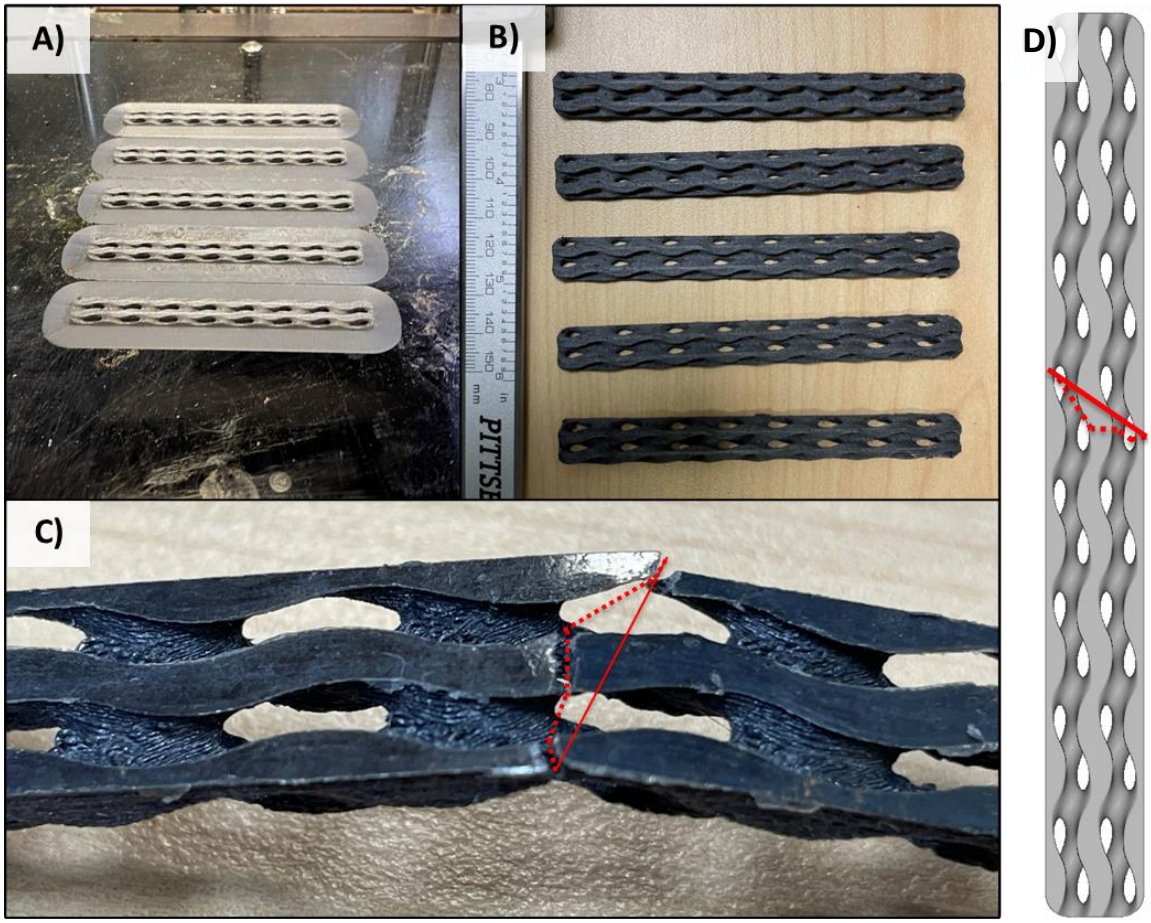

Figure 4.11 – FFF-printed CFR-PEEK gyroid lattices. Images show A) a sample print batch of lattices as printed, B) The sample after removing brim material, and C) the common failure axis observed. The fracture patterns followed a predictable path between the two points of smallest CSA. This failure axis is represented on the illustration in D). The axis is defined by the solid line, while the dashed line tracks the fracture surfaces.

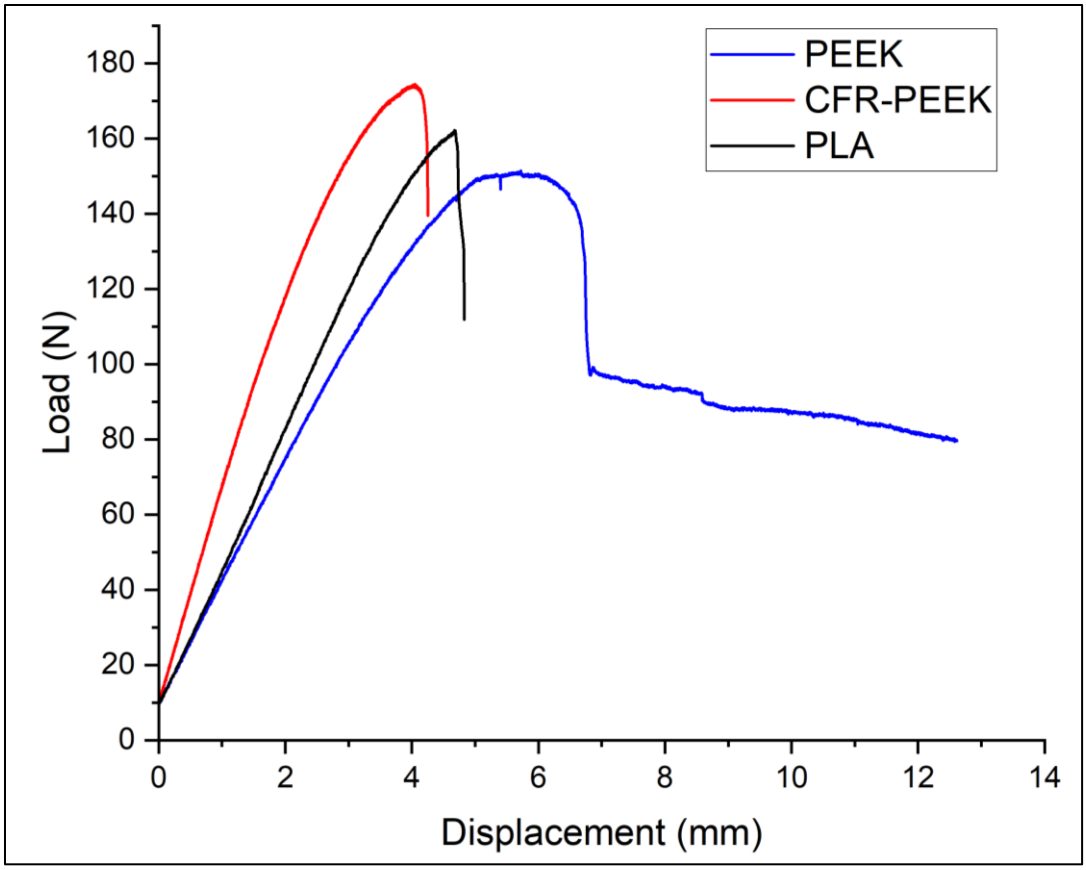

Figure 4.12 – Ductility comparison between PEEK, CFR-PEEK and PLA. Example data selected based on trials with maximum displacement values nearest to the average for the material sample.

in Fig. 4.13. Observation of the fracture surfaces did not show any evidence of debonding between the PLA and the lattice. The failure is assumed to occur first in the lattice then followed immediately by the PLA matrix along the same axis.

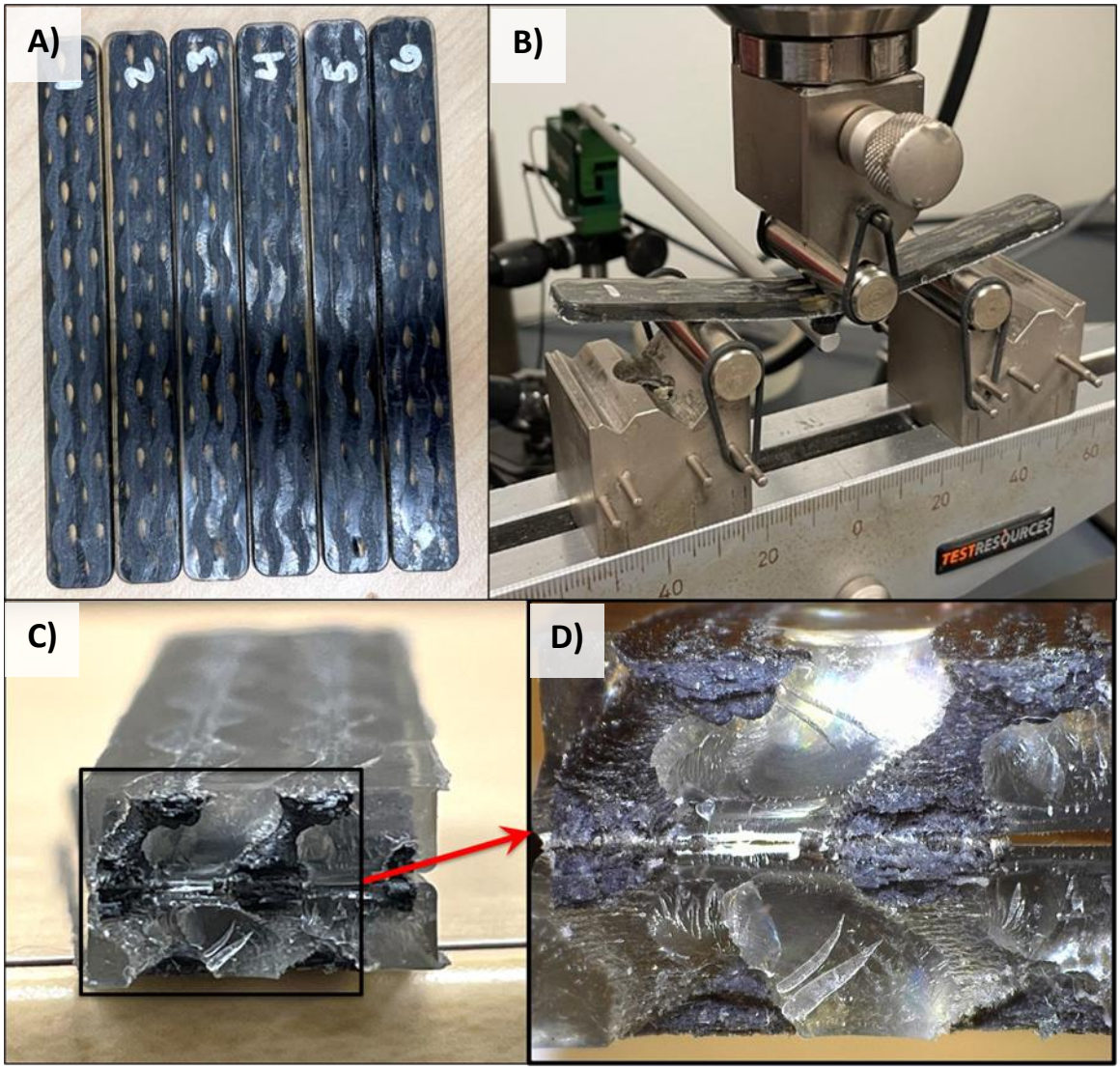

Figure 4.13 – Images show A) OML composite flexural specimens, B) 3-point bend setup during testing. Image C) shows referenced fractures surfaces of folded specimen to show both faces. D) Magnified view of fracture surfaces. The failure images show no failure due to debonding between PLA and the lattice. The composite failure followed the same path as the lattice trials.

CHAPTER FIVE

CONCLUSIONS AND RECOMMENDATIONS

FFF Optimization

Under the current circumstances, the lack of unifying guidance on FFF characterization commonly results in significant variability and limited comparability between studies. The relative novelty of both additive manufacturing and, consequently, the ability to fabricate highly complex cellular structures leaves much to be investigated and improved. There has been an immense amount of research on this topic, and also a growing concern over the FFF characterization issues outlined in previous sections. In the absence of standardized methods, care should be taken to understand the basic process-specific mechanical and material properties which will have an impact on part strength and quality. For the current work, these recommendations focus on improving FFF specimen design and characterization, as well as ILA characterization as a viable method of FFF optimization.

FFF Specimen Design

While there has been an increasing amount of published work highlighting the issues of using molded polymer test methods and geometry for AM specimens, there remains a general lack of education on this matter. Optimizing specimen geometries for the printing process will reduce instances of preliminary or undesirable failures due to improper design (i.e., stress concentrators). A useful categorization of AM characterization is to segregate the methods which attempt to characterize 3D-printed components, and those which seek to optimize the printing process itself. For the former

category, it remains crucial that the print parameters are taken into account- specifically model and layer orientation as they relate to anisotropy of the part. It is necessary, however, to determine the properties of the printed material is as well to fully interpret the mechanics involved in the FFF-component. Developing basic practices, such as ILA tensile testing, will enable a wide range of additive research to improve the validity of the parameters used in these applications. The proposed ILA dogbone geometry results in a specimen with excellent durability, printability, and reduced failure rate compared to D638 specimens. The final version of this model included only 2 bridging layers and was found to be stable through printing and part removal. The drawbacks of this design, however, include potentially long print times for one print batch. For example, the required time to print six ILA specimens at a speed of 30mm/s and 0.1mm is about 10.6 hours. Additionally, while this redesigned specimen improved the likelihood of ILA failures within the desired region, the majority still fell outside of that gauge length.

The first recommendation for improved ILA specimen design is incorporating a hollow gauge length. As a result, the aspect ratio of the specimen will further increase. As an additional benefit, the gauge length can be printed as several layers of concentric walls, improving toolpath efficiency, and reducing the required print time. The next recommendation is the normalization of layer time. It was hypothesized that a possible factor promoting delamination failures within the filleted transition layers, was the increased layer times as the CSA increased, adversely impacting crystallinity and ILA. Analysis and optimization of the G-code could be a useful method to reduce the variance

ILA data. Alternatively, this could also be addressed through the functional grading of infill to normalize the layer time or surface area.

ILA Characterization

ILA characterization was shown to be an effective method to identify the optimal parameters to maximize FFF mechanical properties. The results of the ILA characterization confirmed the findings in the literature recommending high temperature, high speed, and low layer height combinations. PEEK was also determined to be a useful material choice to optimize ILA considering the sensitive nature of the polymer to changes in the thermal environment. As other studies have attempted, reliable improvement to FFF-printed PEEK is dependent on the ability to control polymer crystallization. Based on these properties, PEEK is highly beneficial for any studies investigating the effects of print parameters and thermal annealing on crystallinity, and ILA as a result. An uncolored PEEK filament should be used for these applications to allow for visual inspection of changes in crystallinity. The printer used for this study reached its maximum temperature of 450°C before seeing any adverse effect on part strength. This process could be further refined through a similar study on a semi-crystalline filament with lower thermal requirements, such as PLA.

The present work characterized ILA under quasi-static loading conditions only. It would be worthwhile, however, to investigate how this study might be reproduced under high strain rate conditions to better understand the expected mechanics of FFF structures. Under any condition, however, the use of digital image correlation (DIC) would be highly beneficial to improve characterization. The mechanical response and failure of the

layers in the gauge region under tension is a combination of layer delamination and material strain. The incorporation of DIC would be an ideal solution to monitor and identify specific point of delamination in correlation with the collected data.

Overmolded Lattice Composites

Both the printability and moldability of the CFR-PEEK gyroid lattices was found to be excellent. The design method used could theoretically be expanded to virtually any volume to reinforce. The OML showed SFS, SFM, and SEA properties either comparable to, or greater than the individual materials of the composite. The molded polymer and FFF lattice are mutually beneficial. The gyroid lattice provided significant reinforcement to the polymer, while the overmolded polymer reduced stress concentrations via improved load transfer. The gyroid lattice, as well as other TPMS bodies, are intrinsically compatible structures with the FFF-printing process. The curvature of these bodies provides a CSA, printability, and load transfer typically greater than that in beam-based lattices.

This OML is believed to be a novel composite structure, with immense potential as highly selective reinforcement architecture. For biomedical purposes, this could enable further use of biocompatible and biodegradable polymers to be used in place of metal alternatives. The OML produced in this work could be explored as a potential composite solution to provide mechanical properties comparable to CFR-PEEK, while using half the material, and maintaining the open structure required for TE application following PLA degradation.

Throughout the development of this overmolded composite, no efforts were made to maximize compatibility between polymers, improve interfacial strength, or optimize the mechanical properties of the lattice. This composite structure essentially has the potential that all fiber-reinforced composites do in terms of improved specific strength and stiffness. The distinguishing factor of this OML composite, however, is the high level of control over the design architecture. More in-depth studies of these composites could incorporate different lattice modifications such as functionally graded lattices to tailor the mechanical response. The bolstered fields of additive manufacturing and lattice design provide an ideal groundwork to investigate different forms of this novel structure. The OML composite has potential as an efficient method to reinforce weaker polymers and improve the mechanics of FFF-printed lattices.

LIST OF REFERENCES

[1] A. L. Boskey, “Bone composition: relationship to bone fragility and antiosteoporotic drug effects,” *BoneKEy Rep.*, vol. 2, p. 447, Dec. 2013, doi: 10.1038/bonekey.2013.181.

[2] I. S. Deschamps, G. L. Magrin, R. S. Magini, M. C. Fredel, C. A. M. Benfatti, and J. C. M. Souza, “On the synthesis and characterization of β-tricalcium phosphate scaffolds coated with collagen or poly (D, L-lactic acid) for alveolar bone augmentation,” *Eur. J. Dent.*, vol. 11, no. 4, pp. 496–502, 2017, doi: 10.4103/ejd.ejd_4_17.

[3] X. Lin, S. Patil, Y.-G. Gao, and A. Qian, “The Bone Extracellular Matrix in Bone Formation and Regeneration,” *Front. Pharmacol.*, vol. 11, p. 757, May 2020, doi: 10.3389/fphar.2020.00757.

[4] O. M. Pearson and D. E. Lieberman, “The aging of Wolff’s Law: Ontogeny and responses to mechanical loading in cortical bone,” *Am. J. Phys. Anthropol.*, vol. 125, no. S39, pp. 63–99, 2004, doi: 10.1002/ajpa.20155.

[5] M. G. Mullender and R. Huiskes, “Proposal for the regulatory mechanism of Wolff’s law,” *J. Orthop. Res.*, vol. 13, no. 4, pp. 503–512, Jul. 1995, doi: 10.1002/jor.1100130405.

[6] J. T. Stock, “Wolff’s law (bone functional adaptation),” in *The International Encyclopedia of Biological Anthropology*, W. Trevathan, M. Cartmill, D. Dufour, C. Larsen, D. ORourke, K. Rosenberg, and K. Strier, Eds. Hoboken, NJ, USA: John Wiley & Sons, Inc., 2018, pp. 1–2. doi: 10.1002/9781118584538.ieba0521.

[7] J. Wolff, *The Law of Bone Remodelling*. Berlin, Heidelberg: Springer Berlin Heidelberg, 1986. doi: 10.1007/978-3-642-71031-5.

[8] Bai *et al.*, "Additive Manufacturing of Customized Metallic Orthopedic Implants: Materials, Structures, and Surface Modifications," *Metals*, vol. 9, no. 9, p. 1004, Sep. 2019, doi: 10.3390/met9091004.

[9] K. Prasad *et al.*, "Metallic Biomaterials: Current Challenges and Opportunities," *Materials*, vol. 10, no. 8, p. 884, Jul. 2017, doi: 10.3390/ma10080884.

[10] M. Prakasam, J. Locs, K. Salma-Ancane, D. Loca, A. Largeteau, and L. Berzina-Cimdina, "Biodegradable Materials and Metallic Implants—A Review," *J. Funct. Biomater.*, vol. 8, no. 4, p. 44, Sep. 2017, doi: 10.3390/jfb8040044.

[11] D. L. Millis, "Responses of Musculoskeletal Tissues to Disuse and Remobilization," in *Canine Rehabilitation and Physical Therapy*, Elsevier, 2014, pp. 92–153. doi: 10.1016/B978-1-4377-0309-2.00007-7.

[12] N. Eliaz, "Corrosion of Metallic Biomaterials: A Review," *Materials*, vol. 12, no. 3, p. 407, Jan. 2019, doi: 10.3390/ma12030407.

[13] A. U. Daniels, M. K. O. Chang, K. P. Andriano, and J. Heller, "Mechanical properties of biodegradable polymers and composites proposed for internal fixation of bone," *J. Appl. Biomater.*, vol. 1, no. 1, pp. 57–78, 1990, doi: 10.1002/jab.770010109.

[14] M. Z. Ibrahim, A. A. D. Sarhan, F. Yusuf, and M. Hamdi, "Biomedical materials and techniques to improve the tribological, mechanical and biomedical properties of

orthopedic implants – A review article," *J. Alloys Compd.*, vol. 714, pp. 636–667, Aug. 2017, doi: 10.1016/j.jallcom.2017.04.231.

[15] W.-T. Lee, J.-Y. Koak, Y.-J. Lim, S.-K. Kim, H.-B. Kwon, and M.-J. Kim, "Stress shielding and fatigue limits of poly-ether-ether-ketone dental implants," *J. Biomed. Mater. Res. B Appl. Biomater.*, vol. 100B, no. 4, pp. 1044–1052, 2012, doi: 10.1002/jbm.b.32669.

[16] K. B. Sagomonyants, M. L. Jarman-Smith, J. N. Devine, M. S. Aronow, and G. A. Gronowicz, "The in Vitro Response of Human Osteoblasts to Polyetheretherketone (peek) Substrates Compared to Commercially Pure Titanium," *Biomaterials*, vol. 29, no. 11, pp. 1563–1572, Apr. 2008, doi: 10.1016/j.biomaterials.2007.12.001.

[17] R. Agarwal and A. J. García, "Biomaterial strategies for engineering implants for enhanced osseointegration and bone repair," *Adv. Drug Deliv. Rev.*, vol. 94, pp. 53–62, Nov. 2015, doi: 10.1016/j.addr.2015.03.013.

[18] E. P. Ivanova, K. Bazaka, and R. J. Crawford, *New Functional Biomaterials for Medicine and Healthcare*. Woodhead Publishing, 2014. [Online]. Available: https://www.elsevier.com/books/new-functional-biomaterials-for-medicine-and-healthcare/ivanova/978-1-78242-265-5

[19] N. Ramesh, S. C. Moratti, and G. J. Dias, "Hydroxyapatite–polymer biocomposites for bone regeneration: A review of current trends," *J. Biomed. Mater. Res. B Appl. Biomater.*, vol. 106, no. 5, pp. 2046–2057, 2018, doi: 10.1002/jbm.b.33950.

[20] A. J. T. Teo, A. Mishra, I. Park, Y.-J. Kim, W.-T. Park, and Y.-J. Yoon, "Polymeric Biomaterials for Medical Implants and Devices," *ACS Biomater. Sci. Eng.*, vol. 2, no. 4, pp. 454–472, Apr. 2016, doi: 10.1021/acsbiomaterials.5b00429.

[21] B. D. Ratner, "Polymeric Implants," in *Polymer Science: A Comprehensive Reference*, Elsevier, 2012, pp. 397–411. doi: 10.1016/B978-0-444-53349-4.00230-2.

[22] L. Polo-Corrales, M. Latorre-Esteves, and J. E. Ramirez-Vick, "Scaffold Design for Bone Regeneration," *J. Nanosci. Nanotechnol.*, vol. 14, no. 1, pp. 15–56, Jan. 2014.

[23] B. D. Ulery, L. S. Nair, and C. T. Laurencin, "Biomedical applications of biodegradable polymers," *J. Polym. Sci. Part B Polym. Phys.*, vol. 49, no. 12, pp. 832–864, 2011, doi: 10.1002/polb.22259.

[24] S. Farah, D. G. Anderson, and R. Langer, "Physical and mechanical properties of PLA, and their functions in widespread applications — A comprehensive review," *Adv. Drug Deliv. Rev.*, vol. 107, pp. 367–392, Dec. 2016, doi: 10.1016/j.addr.2016.06.012.

[25] W. Liu *et al.*, "Alkaline biodegradable implants for osteoporotic bone defects—importance of microenvironment pH," *Osteoporos. Int.*, vol. 27, no. 1, pp. 93–104, Jan. 2016, doi: 10.1007/s00198-015-3217-8.

[26] A. Brandao-Burch, J. C. Utting, I. R. Orriss, and T. R. Arnett, "Acidosis Inhibits Bone Formation by Osteoblasts In Vitro by Preventing Mineralization," *Calcif. Tissue Int.*, vol. 77, no. 3, pp. 167–174, Sep. 2005, doi: 10.1007/s00223-004-0285-8.

[27] T. R. Arnett, “Extracellular pH Regulates Bone Cell Function,” *J. Nutr.*, vol. 138, no. 2, pp. 415S-418S, Feb. 2008, doi: 10.1093/jn/138.2.415S.

[28] S. Wickramasinghe, T. Do, and P. Tran, “FDM-Based 3D Printing of Polymer and Associated Composite: A Review on Mechanical Properties, Defects and Treatments,” *Polymers*, vol. 12, no. 7, p. 1529, Jul. 2020, doi: 10.3390/polym12071529.

[29] W. Qin, Y. Li, J. Ma, Q. Liang, and B. Tang, “Mechanical properties and cytotoxicity of hierarchical carbon fiber-reinforced poly (ether-ether-ketone) composites used as implant materials,” *J. Mech. Behav. Biomed. Mater.*, vol. 89, pp. 227–233, Jan. 2019, doi: 10.1016/j.jmbbm.2018.09.040.

[30] S. M. Kurtz and J. N. Devine, “PEEK biomaterials in trauma, orthopedic, and spinal implants,” *Biomaterials*, vol. 28, no. 32, pp. 4845–4869, Nov. 2007, doi: 10.1016/j.biomaterials.2007.07.013.

[31] P. Patel, T. R. Hull, R. W. McCabe, D. Flath, J. Grasmeder, and M. Percy, “Mechanism of Thermal Decomposition of Poly(ether Ether Ketone) (peek) from a Review of Decomposition Studies,” *Polym. Degrad. Stab.*, vol. 95, no. 5, pp. 709–718, May 2010, doi: 10.1016/j.polymdegradstab.2010.01.024.

[32] C.-Y. Liaw, J. W. Tolbert, L. W. Chow, and M. Guvendiren, “Interlayer bonding strength of 3D printed PEEK specimens,” *Soft Matter*, vol. 17, no. 18, pp. 4775–4789, 2021, doi: 10.1039/D1SM00417D.

[33] C. S. Li, C. Vannabouathong, S. Sprague, and M. Bhandari, “The Use of Carbon-Fiber-Reinforced (CFR) PEEK Material in Orthopedic Implants: A Systematic

Review," *Clin. Med. Insights Arthritis Musculoskelet. Disord.*, vol. 8, p. CMAMD.S20354, Jan. 2015, doi: 10.4137/CMAMD.S20354.

[34] V. Shanmugam *et al.*, "Fatigue behaviour of FDM-3D printed polymers, polymeric composites and architected cellular materials," *Int. J. Fatigue*, vol. 143, p. 106007, Feb. 2021, doi: 10.1016/j.ijfatigue.2020.106007.

[35] R. Andrulonis, R. Lovingfoss, and J. Tomblin, "Additive Manufactured Polymer Test Coupons: Issues and Solutions," in *Structural Integrity of Additive Manufactured Parts*, N. Shamsaei, S. Daniewicz, N. Hrabe, S. Beretta, J. Waller, and M. Seifi, Eds. 100 Barr Harbor Drive, PO Box C700, West Conshohocken, PA 19428-2959: ASTM International, 2020, pp. 334–354. doi: 10.1520/STP162020180100.

[36] "3D Printing Market Size, Share | Industry Report, 2021-2028," *Grand View Research*, May 2021. https://www.grandviewresearch.com/industry-analysis/3d-printing-industry-analysis (accessed Feb. 22, 2022).

[37] "3D Printing Market with COVID-19 Impact Analysis by Offering (Printer, Material, Software, Service), Process (Binder Jetting, Direct Energy Deposition, Material Extrusion, Material Jetting, Powder Bed Fusion), Application, Vertical, Technology, and Geography - Global Forecast to 2026," *Markets and Markets*, Feb. 22, 2022. https://www.marketsandmarkets.com/Market-Reports/3d-printing-market-1276.html (accessed Feb. 22, 2022).

[38] J. R. C. Dizon, A. H. Espera, Q. Chen, and R. C. Advincula, “Mechanical characterization of 3D-printed polymers,” *Addit. Manuf.*, vol. 20, pp. 44–67, Mar. 2018, doi: 10.1016/j.addma.2017.12.002.

[39] AMFG, “40+ 3D Printing Industry Stats You Should Know [2021],” *AMFG*, Jan. 14, 2020. https://amfg.ai/2020/01/14/40-3d-printing-industry-stats-you-should-know-2020-redirect/ (accessed Jul. 01, 2022).

[40] C. Y. Park, K. E. Rupel, C. E. Henry, and U. R. Palliyaguru, “Coupon-Level Mechanical Testing for Polymer-Based Additive Manufacturing,” in *Structural Integrity of Additive Manufactured Parts*, N. Shamsaei, S. Daniewicz, N. Hrabe, S. Beretta, J. Waller, and M. Seifi, Eds. 100 Barr Harbor Drive, PO Box C700, West Conshohocken, PA 19428-2959: ASTM International, 2020, pp. 355–366. doi: 10.1520/STP162020180102.

[41] J. Haines, “History of 3D Printing: When Was 3D Printing Invented?,” *All3DP*, Apr. 29, 2022. https://all3dp.com/2/history-of-3d-printing-when-was-3d-printing-invented/ (accessed Jul. 01, 2022).

[42] A. Savini and G. G. Savini, “A short history of 3D printing, a technological revolution just started,” in *2015 ICOHTEC/IEEE International History of High-Technologies and their Socio-Cultural Contexts Conference (HIS^{TEL}CON)*, Aug. 2015, pp. 1–8. doi: 10.1109/HIS^{TEL}CON.2015.7307314.

[43] J. Horvath, *Mastering 3D Printing*. Berkeley, CA: Apress, 2014. doi: 10.1007/978-1-4842-0025-4.

[44] C. W. Hull and S. Gabriel, “Apparatus for production of three-dimensional objects by stereolithography,” p. 16.

[45] M. F. Arif, S. Kumar, K. M. Varadarajan, and W. J. Cantwell, “Performance of Biocompatible PEEK Processed by Fused Deposition Additive Manufacturing,” *Mater. Des.*, vol. 146, pp. 249–259, May 2018, doi: 10.1016/j.matdes.2018.03.015.

[46] “When Was 3D Printing Invented? The History of 3D Printing -,” *BCN3D Technologies*, May 15, 2020. https://www.bcn3d.com/the-history-of-3d-printing-when-was-3d-printing-invented/ (accessed Jul. 01, 2022).

[47] J. Gwamuri, J. E. Poliskey, and J. M. Pearce, “Open Source 3-D Printers: An Appropriate Technology for Developing Communities,” *Proc. 7th Int. Conf. Appropr. Technol.*, 2016, Accessed: Jul. 17, 2022. [Online]. Available: https://hal.archives-ouvertes.fr/hal-02113460

[48] E. Winick, “3D printing’s 30 year history and why it’s popular now,” *Medium*, Jan. 26, 2017. https://medium.com/@erinwinick/3d-printings-30-year-history-and-why-it-is-popular-now-5200ab21a7ed (accessed Jul. 01, 2022).

[49] All3DP, “The Official History of the RepRap Project,” *All3DP*, Apr. 08, 2016. https://all3dp.com/history-of-the-reprap-project/ (accessed Jul. 01, 2022).

[50] D. E. Editors, “Sub-$10,000 3D Printers Near Market,” *Digital Engineering*, Sep. 27, 2007. https://www.digitalengineering247.com/article/sub-10-000-3d-printers-near-market (accessed Jul. 01, 2022).

[51] “Timeline of the 3D Printing History - ASME.” https://www.asme.org/topics-resources/content/infographic-the-history-of-3d-printing (accessed Jul. 01, 2022).

[52] M. Bogers, R. Hadar, and A. Bilberg, “Additive manufacturing for consumer-centric business models: Implications for supply chains in consumer goods manufacturing,” *Technol. Forecast. Soc. Change*, vol. 102, pp. 225–239, Jan. 2016, doi: 10.1016/j.techfore.2015.07.024.

[53] “Fused filament fabrication - RepRap.” https://reprap.org/wiki/Fused_filament_fabrication (accessed Jul. 01, 2022).

[54] S. Ahn, M. Montero, D. Odell, S. Roundy, and P. K. Wright, “Anisotropic material properties of fused deposition modeling ABS,” *Rapid Prototyp. J.*, vol. 8, no. 4, pp. 248–257, Jan. 2002, doi: 10.1108/13552540210441166.

[55] T. J. Gordelier, P. R. Thies, L. Turner, and L. Johanning, “Optimising the FDM additive manufacturing process to achieve maximum tensile strength: a state-of-the-art review,” *Rapid Prototyp. J.*, vol. 25, no. 6, pp. 953–971, Jul. 2019, doi: 10.1108/RPJ-07-2018-0183.

[56] C. Moreau, “State of 3D Printing.” https://www.sculpteo.com/media/ebook/State%20of%203DP%202017_1.pdf (accessed Jun. 28, 2022).

[57] A. A. Stepashkin, D. I. Chukov, F. S. Senatov, A. I. Salimon, A. M. Korsunsky, and S. D. Kaloshkin, “3D-printed PEEK-carbon fiber (CF) composites: Structure and thermal properties,” *Compos. Sci. Technol.*, vol. 164, pp. 319–326, Aug. 2018, doi: 10.1016/j.compscitech.2018.05.032.

[58] M. M. Hanon, R. Marczis, and L. Zsidai, “Anisotropy Evaluation of Different Raster Directions, Spatial Orientations, and Fill Percentage of 3D Printed PETG

Tensile Test Specimens," *Key Eng. Mater.*, vol. 821, pp. 167–173, Sep. 2019, doi: 10.4028/www.scientific.net/KEM.821.167.

[59] C. Casavola, A. Cazzato, V. Moramarco, and C. Pappalettere, "Orthotropic mechanical properties of fused deposition modelling parts described by classical laminate theory," *Mater. Des.*, vol. 90, pp. 453–458, Jan. 2016, doi: 10.1016/j.matdes.2015.11.009.

[60] N. Chantarapanich, P. Puttawibul, K. Sitthiseripratip, S. Sucharitpwatskul, and S. Chantaweroad, "Study of the mechanical properties of photo-cured epoxy resin fabricated by stereolithography process," p. 9, 2013.

[61] C. Schmidleithner, S. Malferrari, R. Palgrave, D. Bomze, M. Schwentenwein, and D. M. Kalaskar, "Application of high resolution DLP stereolithography for fabrication of tricalcium phosphate scaffolds for bone regeneration," *Biomed. Mater.*, vol. 14, no. 4, p. 045018, Jun. 2019, doi: 10.1088/1748-605X/ab279d.

[62] C. Pan, Y. Han, and J. Lu, "Design and Optimization of Lattice Structures: A Review," *Appl. Sci.*, vol. 10, no. 18, p. 6374, Sep. 2020, doi: 10.3390/app10186374.

[63] I. Maskery *et al.*, "Insights into the mechanical properties of several triply periodic minimal surface lattice structures made by polymer additive manufacturing," *Polymer*, vol. 152, pp. 62–71, Sep. 2018, doi: 10.1016/j.polymer.2017.11.049.

[64] "Guide to Lattice Structures in Additive Manufacturing," *nTopology*, Apr. 28, 2022. https://ntopology.com/blog/guide-to-lattice-structures-in-additive-manufacturing/ (accessed Jun. 06, 2022).

[65] J. Sienkiewicz, P. Płatek, F. Jiang, X. Sun, and A. Rusinek, “Investigations on the Mechanical Response of Gradient Lattice Structures Manufactured via SLM,” *Metals*, vol. 10, no. 2, p. 213, Feb. 2020, doi: 10.3390/met10020213.

[66] H.-Y. Lei, J.-R. Li, Z.-J. Xu, and Q.-H. Wang, “Parametric design of Voronoi-based lattice porous structures,” *Mater. Des.*, vol. 191, p. 108607, Jun. 2020, doi: 10.1016/j.matdes.2020.108607.

[67] S. Gómez, M. D. Vlad, J. López, and E. Fernández, “Design and properties of 3D scaffolds for bone tissue engineering,” *Acta Biomater.*, vol. 42, pp. 341–350, Sep. 2016, doi: 10.1016/j.actbio.2016.06.032.

[68] G. Wang *et al.*, “Design and Compressive Behavior of Controllable Irregular Porous Scaffolds: Based on Voronoi-Tessellation and for Additive Manufacturing,” *ACS Biomater. Sci. Eng.*, vol. 4, no. 2, pp. 719–727, Feb. 2018, doi: 10.1021/acsbiomaterials.7b00916.

[69] S. Kechagias, R. N. Oosterbeek, M. J. Munford, S. Ghouse, and J. R. T. Jeffers, “Controlling the mechanical behaviour of stochastic lattice structures: The key role of nodal connectivity,” *Addit. Manuf.*, vol. 54, p. 102730, Jun. 2022, doi: 10.1016/j.addma.2022.102730.

[70] A. H. Reddy, S. Davuluri, and D. Boyina, “3D Printed Lattice Structures: A Brief Review,” in *2020 IEEE 10th International Conference Nanomaterials: Applications & Properties (NAP)*, Sumy, Ukraine, Nov. 2020, pp. 02SAMA10-1-02SAMA10-5. doi: 10.1109/NAP51477.2020.9309680.

[71] D. W. Abueidda, M. Elhebeary, C.-S. (Andrew) Shiang, S. Pang, R. K. Abu Al-Rub, and I. M. Jasiuk, “Mechanical properties of 3D printed polymeric Gyroid cellular structures: Experimental and finite element study,” *Mater. Des.*, vol. 165, p. 107597, Mar. 2019, doi: 10.1016/j.matdes.2019.107597.

[72] S. C. Kapfer, S. T. Hyde, K. Mecke, C. H. Arns, and G. E. Schröder-Turk, “Minimal Surface Scaffold Designs for Tissue Engineering,” *Biomaterials*, vol. 32, no. 29, pp. 6875–6882, Oct. 2011, doi: 10.1016/j.biomaterials.2011.06.012.

[73] G. K. Maharjan, S. Z. Khan, S. H. Riza, and S. Masood, “Compressive Behaviour of 3D Printed Polymeric Gyroid Cellular Lattice Structure,” *IOP Conf. Ser. Mater. Sci. Eng.*, vol. 455, p. 012047, Dec. 2018, doi: 10.1088/1757-899X/455/1/012047.

[74] R. Vrana, D. Koutny, and D. Palousek, “Impact Resistance of Different Types of Lattice Structures Manufactured by Slm,” *MM Sci. J.*, vol. 2016, no. 06, pp. 1579–1585, Dec. 2016, doi: 10.17973/MMSJ.2016_12_2016186.

[75] S. N. Khaderi, V. S. Deshpande, and N. A. Fleck, “The Stiffness and Strength of the Gyroid Lattice,” *Int. J. Solids Struct.*, vol. 51, no. 23–24, pp. 3866–3877, Nov. 2014, doi: 10.1016/j.ijsolstr.2014.06.024.

[76] A. S. Whitehead, “Triply Periodic Minimal Surfaces,” *WeWantToLearn.net*, Feb. 03, 2019. https://wewanttolearn.wordpress.com/2019/02/03/triply-periodic-minimal-surfaces/ (accessed Jun. 07, 2022).

[77] J. Hussmo and R. Schröder, “Experiments, analysis and an application of 3D-printed gyroid structures,” 2020.

[78] O. Al-Ketan and R. K. Abu Al-Rub, “MSLattice: A free software for generating uniform and graded lattices based on triply periodic minimal surfaces,” *Mater. Des. Process. Commun.*, vol. 3, no. 6, Dec. 2021, doi: 10.1002/mdp2.205.

[79] P. Habibovic, H. Yuan, C. M. van der Valk, G. Meijer, C. A. van Blitterswijk, and K. de Groot, “3D microenvironment as essential element for osteoinduction by biomaterials,” *Biomaterials*, vol. 26, no. 17, pp. 3565–3575, Jun. 2005, doi: 10.1016/j.biomaterials.2004.09.056.

[80] M. P. Nikolova and M. S. Chavali, “Recent advances in biomaterials for 3D scaffolds: A review,” *Bioact. Mater.*, vol. 4, pp. 271–292, Dec. 2019, doi: 10.1016/j.bioactmat.2019.10.005.

[81] A. Selvam, S. Mayilswamy, R. Whenish, R. Velu, and B. Subramanian, “Preparation and Evaluation of the Tensile Characteristics of Carbon Fiber Rod Reinforced 3D Printed Thermoplastic Composites,” *J. Compos. Sci.*, vol. 5, no. 1, p. 8, Dec. 2020, doi: 10.3390/jcs5010008.

[82] N. Naveed, “Investigate the effects of process parameters on material properties and microstructural changes of 3D-printed specimens using fused deposition modelling (FDM),” *Mater. Technol.*, vol. 36, no. 5, pp. 317–330, Apr. 2021, doi: 10.1080/10667857.2020.1758475.

[83] A. Alafaghani, A. Qattawi, B. Alrawi, and A. Guzman, “Experimental Optimization of Fused Deposition Modelling Processing Parameters: A Design-for-Manufacturing Approach,” *Procedia Manuf.*, vol. 10, pp. 791–803, 2017, doi: 10.1016/j.promfg.2017.07.079.

[84] A. Garg and A. Bhattacharya, “An Insight to the Failure of FDM Parts Under Tensile Loading: Finite Element Analysis and Experimental Study,” *Int. J. Mech. Sci.*, vol. 120, pp. 225–236, Jan. 2017, doi: 10.1016/j.ijmecsci.2016.11.032.

[85] J. M. Chacón, M. A. Caminero, E. García-Plaza, and P. J. Núñez, “Additive Manufacturing of PLA Structures Using Fused Deposition Modelling: Effect of Process Parameters on Mechanical Properties and Their Optimal Selection,” *Mater. Des.*, vol. 124, pp. 143–157, Jun. 2017, doi: 10.1016/j.matdes.2017.03.065.

[86] M. Rinaldi, T. Ghidini, F. Cecchini, A. Brandao, and F. Nanni, “Additive layer manufacturing of poly (ether ether ketone) via FDM,” *Compos. Part B Eng.*, vol. 145, pp. 162–172, Jul. 2018, doi: 10.1016/j.compositesb.2018.03.029.

[87] T. Yao, J. Ye, Z. Deng, K. Zhang, Y. Ma, and H. Ouyang, “Tensile Failure Strength and Separation Angle of FDM 3D Printing PLA Material: Experimental and Theoretical Analyses,” *Compos. Part B Eng.*, vol. 188, p. 107894, May 2020, doi: 10.1016/j.compositesb.2020.107894.

[88] Y. Zhao, K. Zhao, Y. Li, and F. Chen, “Mechanical characterization of biocompatible PEEK by FDM,” *J. Manuf. Process.*, vol. 56, pp. 28–42, Aug. 2020, doi: 10.1016/j.jmapro.2020.04.063.

[89] S. Wang, Y. Ma, Z. Deng, S. Zhang, and J. Cai, “Effects of Fused Deposition Modeling Process Parameters on Tensile, Dynamic Mechanical Properties of 3D Printed Polylactic Acid Materials,” *Polym. Test.*, vol. 86, p. 106483, Jun. 2020, doi: 10.1016/j.polymertesting.2020.106483.

[90] S. Xiaoyong, C. Liangcheng, M. Honglin, G. Peng, B. Zhanwei, and L. Cheng, "Experimental Analysis of High Temperature PEEK Materials on 3D Printing Test," in *2017 9th International Conference on Measuring Technology and Mechatronics Automation (ICMTMA)*, Jan. 2017, pp. 13–16. doi: 10.1109/ICMTMA.2017.0012.

[91] T. M. Lazović and M. S. Stojanović, "Preparation of specimens for standard tensile testing of plastic materials for FDM 3D printing," no. 5, p. 4, 2021.

[92] "Tensile Testing for 3D Printing Materials." https://www.protolabs.com/resources/blog/tensile-testing-for-3d-printing-materials/ (accessed Jul. 09, 2022).

[93] T. Hyatt, R. Martin, and R. Fields, "Design of Coupons and Test Methodology for Orthotropic Characterization of FFF-Processed Ultem 9085," in *Structural Integrity of Additive Manufactured Materials & Parts*, N. Shamsaei and M. Seifi, Eds. 100 Barr Harbor Drive, PO Box C700, West Conshohocken, PA 19428-2959: ASTM International, 2020, pp. 176–187. doi: 10.1520/STP163120190126.

[94] "Committee F42 on Additive Manufacturing Technologies." https://www.astm.org/get-involved/technical-committees/committee-f42 (accessed Feb. 17, 2022).

[95] "Committee F42 Subcommittees." https://www.astm.org/get-involved/technical-committees/committee-f42/subcommittee-f42 (accessed Feb. 17, 2022).

[96] “Material Extrusion Processes,” *ASTM Standardization News*, Dec. 13, 2021. https://sn.astm.org/?q=update/material-extrusion-processes-jf22.html (accessed Feb. 17, 2022).

[97] F42 Committee, “ASTM 52900-15 - Standard Terminology for Additive Manufacturing – General Principles – Terminology.”

[98] F42 Committee, “ASTM 52921-13 - Standard Terminology for Additive Manufacturing—Coordinate Systems and Test Methodologies.pdf.”

[99] F42 Committee, “ASTM 52950 - Additive manufacturing — General principles — Overview of data processing.pdf.”

[100] F42 Committee, “ASTM F2971-13 - Practice for Reporting Data for Test Specimens Prepared by Additive Manufacturing,” ASTM International. doi: 10.1520/F2971-13R21.

[101] F42 Committee, “ASTM 52903-1 - Additive manufacturing — Material extrusion-based additive manufacturing of plastic materials — Part 1: Feedstock materials.”

[102] F42 Committee, “ASTM 52903-2 - Additive manufacturing — Material extrusion-based additive manufacturing of plastic materials — Part 2_ Process equipment.pdf.”

[103] Z. Abidin *et al.*, “Optimization of FDM 3D Printing Process Parameter for Improving Porosity Accuracy of PLA Scaffold:,” presented at the 4th Forum in Research, Science, and Technology (FIRST-T1-T2-2020), Palembang, Indonesia, 2021. doi: 10.2991/ahe.k.210205.028.

[104] R. Dua, Z. Rashad, J. Spears, G. Dunn, and M. Maxwell, “Applications of 3D-Printed PEEK via Fused Filament Fabrication: A Systematic Review,” *Polymers*, vol. 13, no. 22, p. 4046, Nov. 2021, doi: 10.3390/polym13224046.

[105] E. Alonso-Rodriguez, J. L. Cebrián, M. J. Nieto, J. L. Del Castillo, J. Hernández-Godoy, and M. Burgueño, “Polyetheretherketone custom-made implants for craniofacial defects: Report of 14 cases and review of the literature,” *J. Cranio-Maxillofac. Surg.*, vol. 43, no. 7, pp. 1232–1238, Sep. 2015, doi: 10.1016/j.jcms.2015.04.028.

[106] E. L. Steinberg, E. Rath, A. Shlaifer, O. Chechik, E. Maman, and M. Salai, “Carbon fiber reinforced PEEK Optima—A composite material biomechanical properties and wear/debris characteristics of CF-PEEK composites for orthopedic trauma implants,” *J. Mech. Behav. Biomed. Mater.*, vol. 17, pp. 221–228, Jan. 2013, doi: 10.1016/j.jmbbm.2012.09.013.

[107] I. V. Panayotov, V. Orti, F. Cuisinier, and J. Yachouh, “Polyetheretherketone (peek) for Medical Applications,” *J. Mater. Sci. Mater. Med.*, vol. 27, no. 7, Jul. 2016, doi: 10.1007/s10856-016-5731-4.

[108] S. Singh, C. Prakash, and S. Ramakrishna, “3D printing of polyether-ether-ketone for biomedical applications,” *Eur. Polym. J.*, vol. 114, pp. 234–248, May 2019, doi: 10.1016/j.eurpolymj.2019.02.035.

[109] C. Yang, X. Tian, D. Li, Y. Cao, F. Zhao, and C. Shi, “Influence of Thermal Processing Conditions in 3d Printing on the Crystallinity and Mechanical Properties

of PEEK Material," *J. Mater. Process. Technol.*, vol. 248, pp. 1–7, Oct. 2017, doi: 10.1016/j.jmatprotec.2017.04.027.

[110] K. Rodzeń, E. Harkin-Jones, M. Wegrzyn, P. K. Sharma, and A. Zhigunov, "Improvement of the layer-layer adhesion in FFF 3D printed PEEK/carbon fibre composites," *Compos. Part Appl. Sci. Manuf.*, vol. 149, p. 106532, Oct. 2021, doi: 10.1016/j.compositesa.2021.106532.

[111] X. Tardif *et al.*, "Experimental Study of Crystallization of Polyetheretherketone (PEEK) Over a Large Temperature Range Using a Nano-Calorimeter," *Polym. Test.*, vol. 36, pp. 10–19, Jun. 2014, doi: 10.1016/j.polymertesting.2014.03.013.

[112] L. Ryan, "Utilization of Lattice Structures for Increased Interface Strength in Overmolded Silicone and Additively Manufactured Parts," MS, Pennsylvania State University, 2020. Accessed: Jun. 01, 2022. [Online]. Available: https://etda.libraries.psu.edu/files/final_submissions/21322

[113] S. Verma, C.-K. Yang, C.-H. Lin, and J. Y. Jeng, "Additive manufacturing of lattice structures for high strength mechanical interlocking of metal and resin during injection molding," *Addit. Manuf.*, vol. 49, p. 102463, Jan. 2022, doi: 10.1016/j.addma.2021.102463.

[114] "Ingeo Biopolymer 4043D Technical Data Sheet," p. 3.

[115] "CarbonX^{TM} Carbon Fiber Reinforced PEEK+CF10 3D Printing Filament | Extreme Performance PEEK Filament." https://www.3dxtech.com/product/carbonx-peek-cf10/ (accessed Jul. 11, 2022).

[116] D20 Committee, “ASTM D618 - Practice for Conditioning Plastics for Testing,” ASTM International. doi: 10.1520/D0618-21.

[117] “ASTM D790 Flexural Test Mold,” *APSX LLC*. https://www.apsx.com/astm-d790-flexural-test-mold (accessed Jan. 12, 2022).

VITA

Ryan Ogle was born and raised in Knoxville, Tennessee. Through his time in high school, he became aware of his predilection for STEM subjects and was encouraged to apply these interests in the pursuit of an engineering degree. He was additionally interested in biology and healthcare, and through researching various engineering programs learned for the first time of biomedical engineering. He chose to attend the University of Tennessee, Knoxville due to proximity to family and it being one of the only schools in the state at the time with a biomedical program. Through his experience in ungraduated research at the Fibers and Composites Manufacturing Facility, he developed an interest in applying the same composite solutions to solve medical problems. After graduation, he will be seeking to further this desire to develop advanced biomaterial composites.